7. THREE DIMENSIONAL SYNTHESIZED MODEL

7.1 GEOLOGY

A three dimensional model of the geology of the Transvaal Sequence has been constructed and is shown in Figures 37(a) and (b). The model shows the basin-like behaviour of the Transvaal sequence, but in terms of the DNAPL pools and the movement of the historic pools this model is only of academic importance.

Figure 38 represents a montage of (a) a cross section through the model and (b) a view from the north looking southwards.

7.2 OVERBURDEN LAYER

Since tar is dense it will move downward by the force of gravity and to predict where it will be located the nature of the solid bedrock profile has to be known. Both unweathered shale and quartzite will provide a natural barrier to the tar. The tar may, however, proceed in crevasses and joints to some depth in a partly decomposed rock. Problem areas will occur where the tar occurs below the water table, so areas with overburden thickness of more than 10m and tar occurring at the overburden fresh rock interface in these deeper weather parts, are the ones to be identified. It is possible to obtain the overburden thickness from the transient electromagnetic soundings by taking the thickness of the first layer and equating that with the overburden thickness. It is an approximation but will provide the correct trend. To this data the borehole information that was available to the author was added. Figure 39 depicts the overburden thickness as determined from the transient EM soundings and identified from borehole data. From the Figure it is evident that overburden thickness is quite small, west of Dam 10, but then increases locally eastwards in the area where tar deposition is suspected. There it reaches a maximum of 10m. Further south a local maximum thickness of overburden is also encountered which reaches 15m where coal tar has subsequently been encountered (see Figure 36).

Other areas where quite deep depth to bedrock is found is north of the fault line and on the east-west striking dyke.

7.3 POLLUTION PATHWAYS

There are 3 possible DNAPL pollution pathways in the area. The first is by having tar below the water level in a local depression in the solid rock. The second is if tar leaked into the fault that crosses the area of interest. The fault extends right through the Transvaal Sequence. Unfortunately the fault also underlies one of the waste dumps. The third way is if tar occurs across the east-west dyke that also crosses the upper waste rock dump. Figure 40 indicates the vulnerable areas that have to be investigated where the IP effect coincides with areas of deeper weathering (> 10m) marked no 3. Very small IP effects were recorded at the upper waste rock dump. Water samples along the periphery of the dyke marked area 1 would indicate if hydrocarbons are present here. The fault unfortunately cuts through the ISCOR property creating many opportunities for foreign material moving into the ground water. The vulnerable area here is marked no 2 on Figure 40.

8 CONCLUSIONS

8.1 The geology of the area is fairly well understood and a model of the regional geology is presented, augmented by geophysical information. For the spread of soluble DNAPL compounds, the presence of a fault that lies below the steel mill and more important, below one of the slag dumps, could have serious implications. Since the fault is present through the whole of the Transvaal Sequence, it connects the surface with the dolomite 900m below surface.

8.2 The high resolution aeromagnetic data set, confirmed that only one dyke is present in the area of interest. A clear displacement in the dyke indicates that the left lateral strike fault probably also caused this displacement.

8.3 The high resolution aeromagnetic data is quite noisy due to man made effects and the effect of diabase sills that intruded into the Transvaal Sequence are not visible in the data.

8.4 The radiometric data indicated that the slag dumps to the north of the steel mill are at an elevated radiometric level and are Th and U rich with values about 6 times the natural background. Elevated Th and U levels were also recorded the built-up areas of Vanderbijlpark and it could be that slag from the steel mill was used in the mortar or brick making process.

8.5 The reflection seismic survey indicated that the Chuniespoort dolomite is about 1.2km below the present day surface and is in accordance with the gravity models. Except for the fault which can introduce soluble tar components into the dolomite, this unit is unaffected by tar that lies near the surface in a weathered rock depression.

8.6 Ground water pollution by DNAPL's can be caused by three mechanisms namely mechanism 1 is where the tar exists in deeper weathered zones that lie below the water table and soluble components of the DNAPL compounds dissolve in the water. Mechanism 2 involves the movement of tar in the left lateral strike fault. Mechanism 3 is tar moving along the dyke that also underlies the existing waste dump.

8.7 An experiment was undertaken to determine whether the tar occurrences cause a recognizable IP effect on transient EM soundings. The presence of such material can clearly be demonstrated theoretically but in practise only mixed results were achieved. On estimation 65 percent of the soundings that indicated the IP effect could be confirmed with drilling that DNAPL material were indeed present. Man made electrical noise contributed to the false signals received and a third phenomenon which is not understood yet caused the remainder of the false anomalies. These false anomalies were mostly situated to the north of the existing waste dump.

9 RECOMMENDATIONS

9.1 The locality of the fault be established through drilling and that the water in the fault be tested for the presence of hydro carbons.

9.2 The periphery of the fault where it underlies the existing waste dump be drilled and tested for the presence of hydrocarbons in the ground water.

9.3 The investigation by drilling of the identified areas with IP effect, west of Dam 10.

10 REFERENCES

Bosch, P. (1997). Geological map of the 2627 DB Vereeniging sheet. Publication of the Council for Geoscience.

Duval, J.S. (1983). Composite colour images of aerial gamma-ray spectrometric data. Geophys 48, p722-735.

Hofgaard, J. (1997). A new processing technique for airborne gamma-ray spectrometer data (noise adjusted singular value decomposition). In Am Nucl. Soc. Sixth topical meeting on Emergency Preparedness and Response, pages 22-25, San Francisco, April 1997.

Kamenetsky, F.V., Novikov, P.V. and Timofeev, V.M. (1995). O vozmozhnosti fiziches-kogo modelirovaniya elektromagnitnogo polya v provodyatschei polarizuyu-tscheisya srede. Izvestiya AN RAN: seriya Fizika Zemli, 5: 46-54 (in Russian).

Zadorozhnaya, V. and Bessonov, A. (2001). The IP effect as indicator of hydrocarbon pollution in ground water. Abstract. XXVI General Assembly, European Geophysical Society, Nice.

Dr E H Stettler (PrSciNat)
COUNCIL FOR GEOSCIENCE

A GEOPHYSICAL INVESTIGATION OF THE AREA SURROUNDING THE VANDERBILJPARK STEEL MILL

VOLUME 2 – FIGURES AND APPENDICES

BY:

E.H. STETTLER

REPORT NUMBER: 2001-0238

CONTENTS

VOLUME 2

APPENDIX A

FIGURES

APPENDIX A

FIGURES

1. General locality of the area investigated as taken from the 2627DM Vereeniging, 1:50 000 topo sheet
2. (a) Aerial photograph depicting the latest infrastructure. LO 27 X and Y co-ordinates were interchanged and multiplied by -1. to establish a right handed Cartesian coordinate system. See Figure 2(b) for identifying land marks.
   (b) Aerial photograph with salient features highlighted to facilitate orientation on the following images. Both the X and Y co-ordinates in LO 27 have been interchanged and multiplied by -1. to fit into a right handed Cartesian co-ordinate system.
3. (a) Geology of the investigated area enhanced by geophysical data.
   (b) Geology of the investigated area in relation to the infrastructure.
   (c) Stratigraphic sequence for 2627 DB Vereeniging.
4. Classification of outcropping rocks and soil material in the investigated area in terms of geotechnical parameters.
5. Total field aeromagnetic map with artificial sun shading from the north. Warm colours signify magnetic highs.
6. Qualitative interpretation of the magnetic data.
7. Colour coded Potassium concentration map, the maximum concentration is 8 per cent, signified by the areas coloured deep red.
8. Colour coded Uranium concentration map in ppm. The highest concentration is 21 ppm and occurs over the slag dumps, the steel works and Vanderbijlpark. The maximum concentration coloured dark red.
9. Colour coded Thorium concentration map in ppm. The highest concentration is 38 ppm and occurs over the slag dump, the steel works and Vanderbijlpark.
10. Colour coded gamma-ray Total Count map. The map summarizes the contributions of all radiometric sources.
11. Ternary plot with magenta, cyan and yellow representing K, U, Th respectively.
12. Radiometric ternary map with geology overlay.
13. Digital terrain model as determined from the airborne geophysical survey. The infrastructure map is overlain.
14. Representation of light absorption and emission for band 1 (1.0 to 1.2 micron) of the airborne Near Infra Ref (NIR) spectral profiler. Geology outline is overlain.
15. Representation of light absorption and emission for band 2 (1.2 to 1.4 micron) of the airborne Near Infra Red (NIR) spectral profiler. Geology outline is overlain.

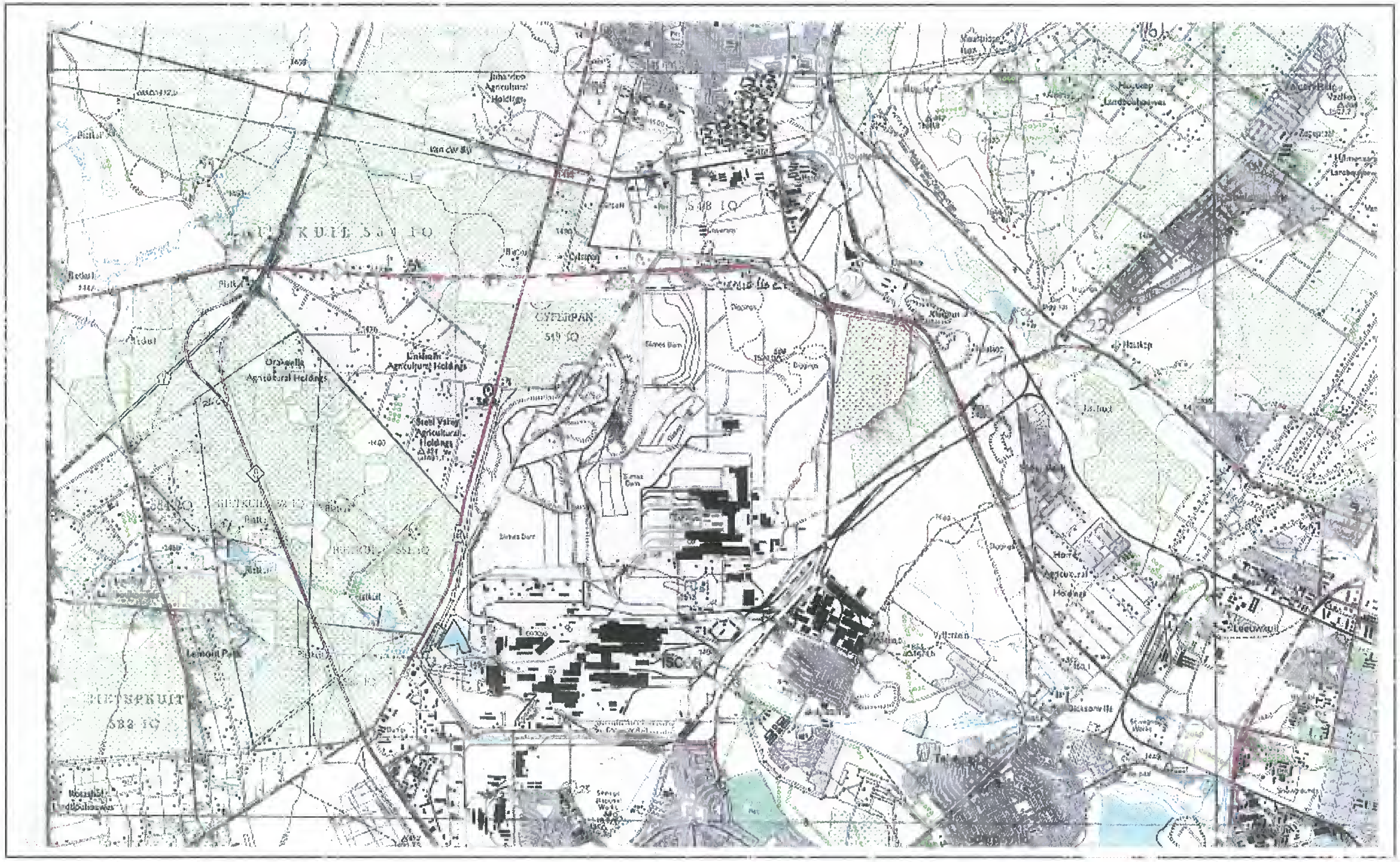

Figure 1. General locality of the area investigated as taken from the 2627DB Vereeniging 1:50 000 topo sheet .

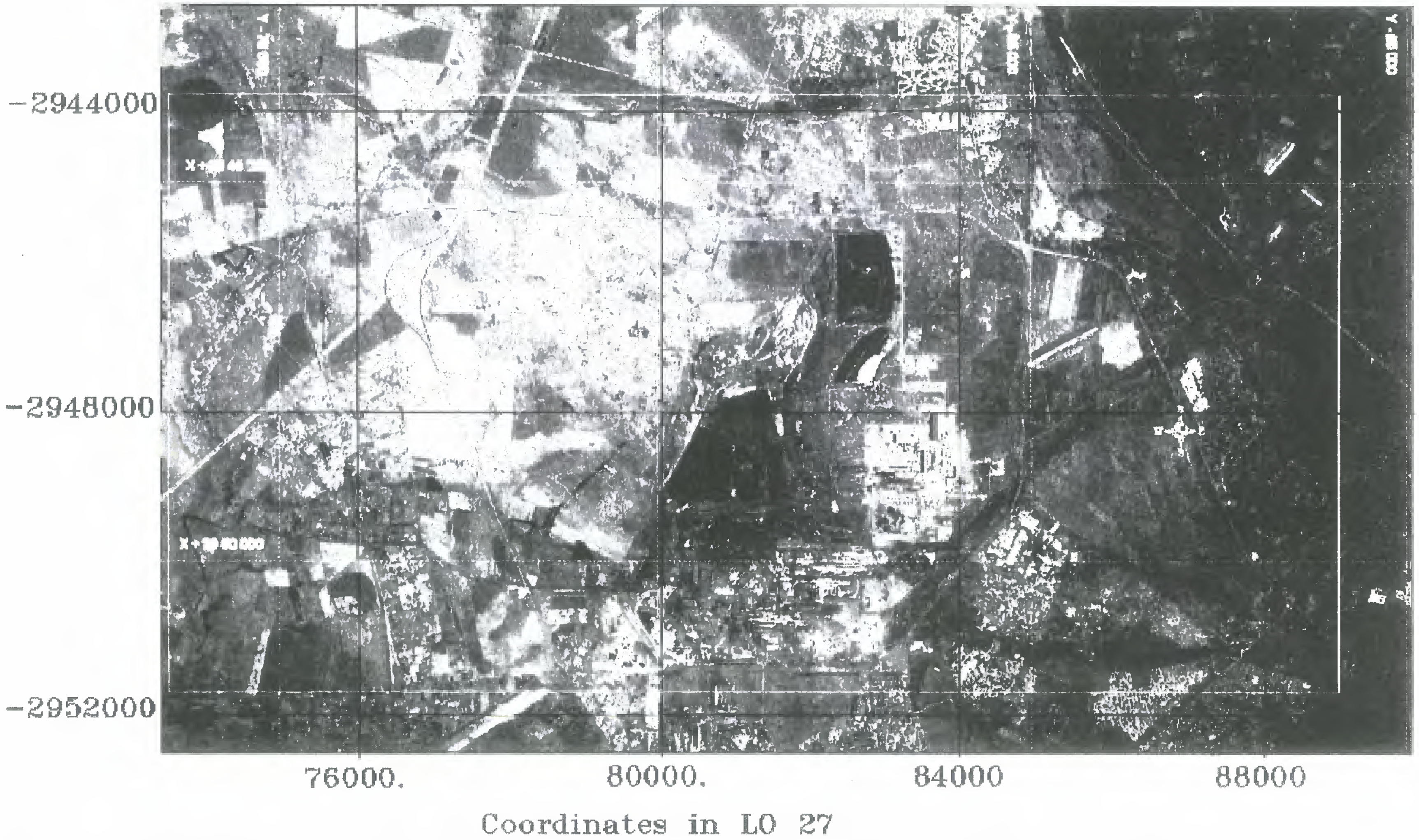

Figure 2 a. Aerial photograph depicting the latest infra structure. LO 27 x and y coordinates were interchanged and multiplied by –1 to establish a right-handed Cartesian coordinate system. See Figure 2b for identifying landmarks.

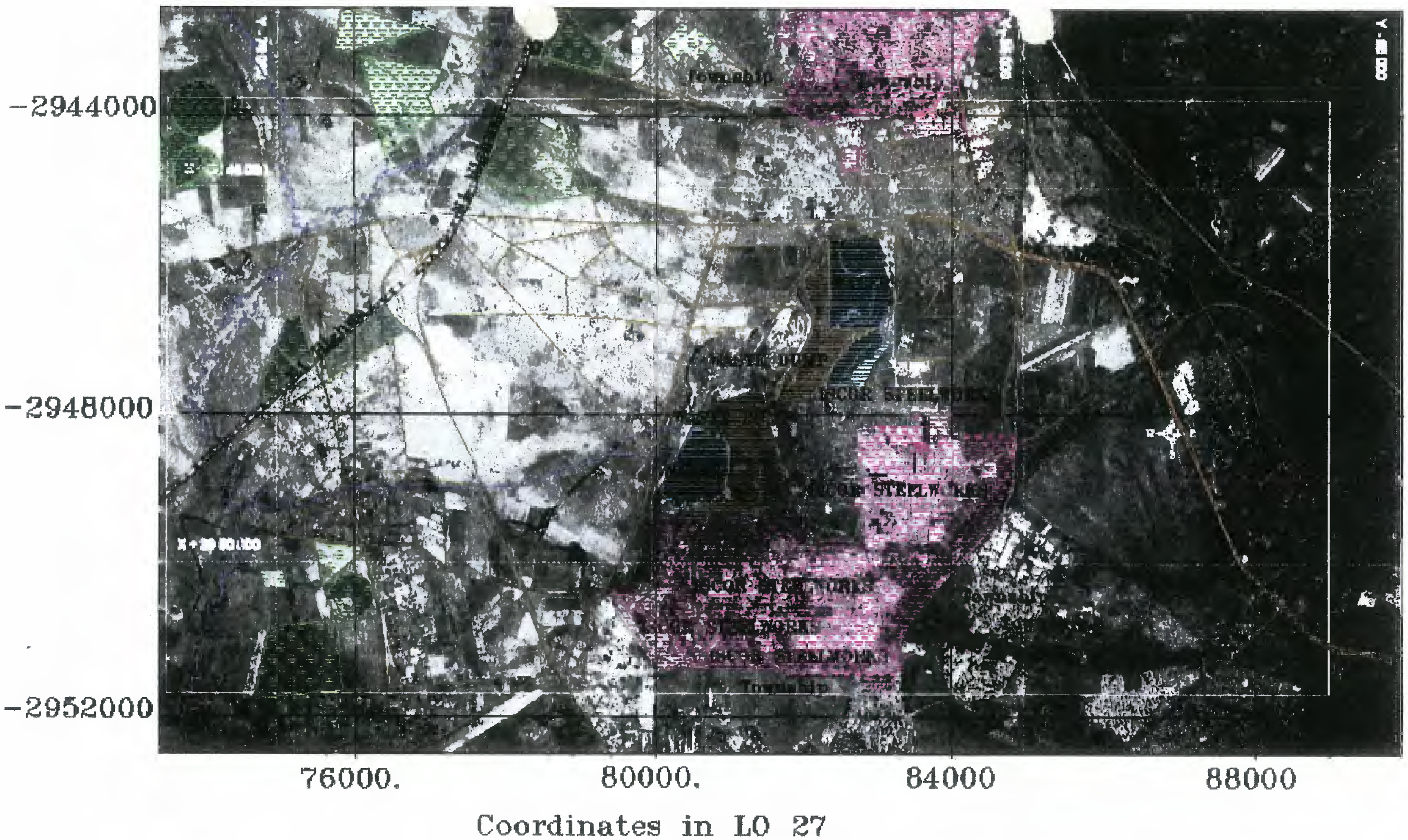

Figure 2 b. Aerial photograph with salient features highlighted to facilitate orientation on following images . Both the x and y coordinates of L O 27have been interchanged and multiplied by –1. 0 to fit into a right-handed Cartesian coordinate system.

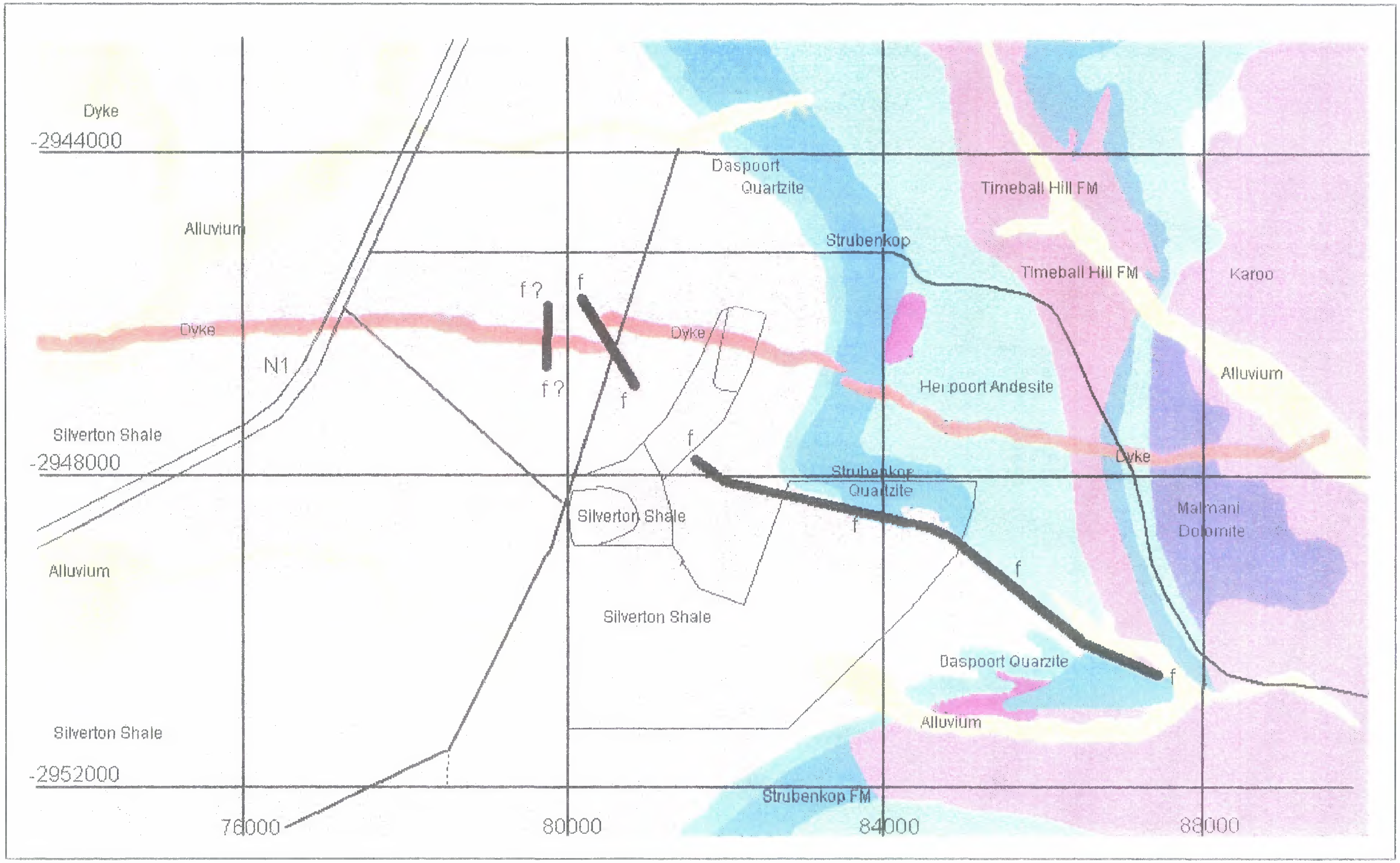

Figure 3(a). Geology of the investigated area enhanced by geophysical data.

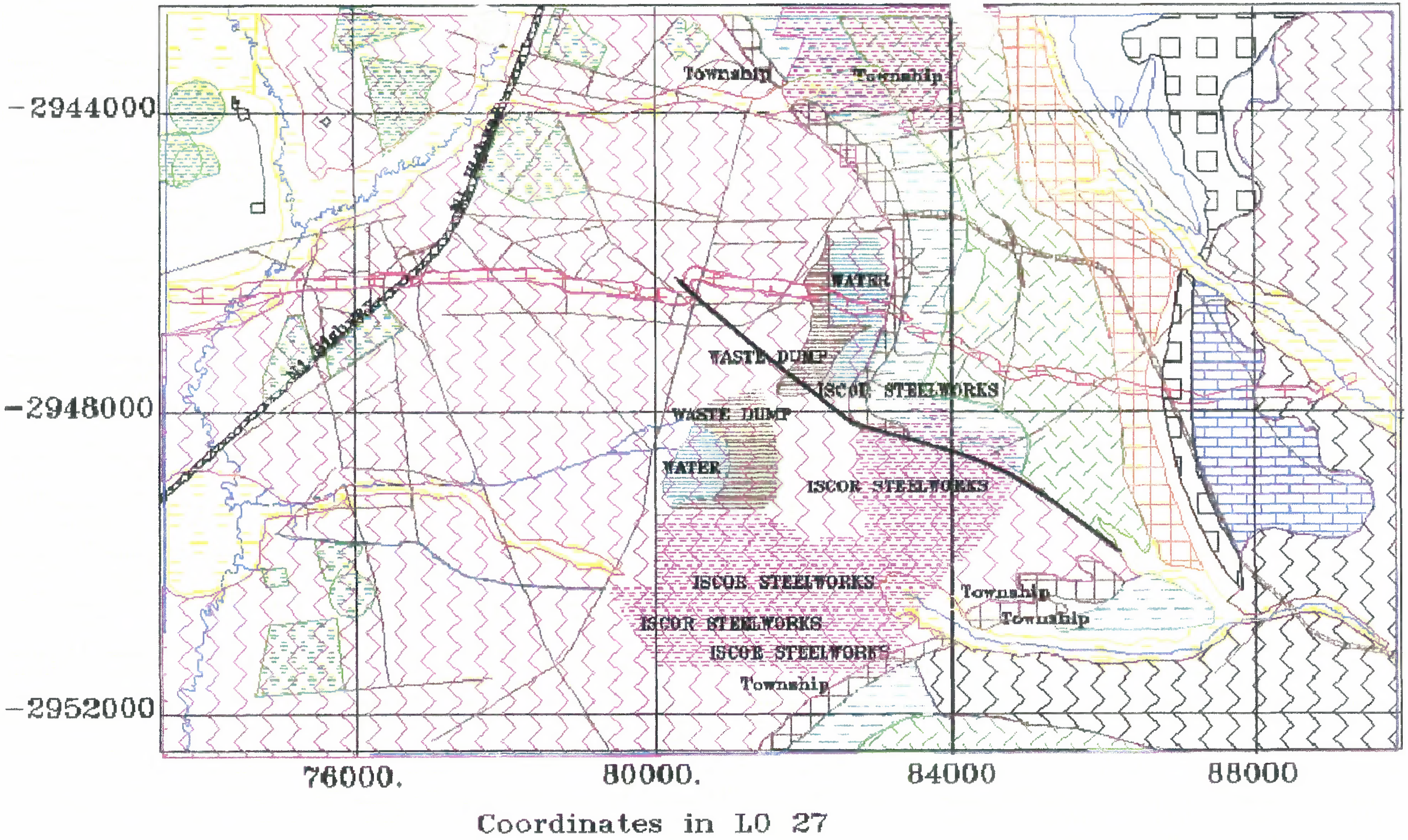

Figure 3(b). Geology of the investigated area in relation to the infrastructure.

STRATIGRAPHIC SEQUENCE
FOR 2627DB VEREENIGING

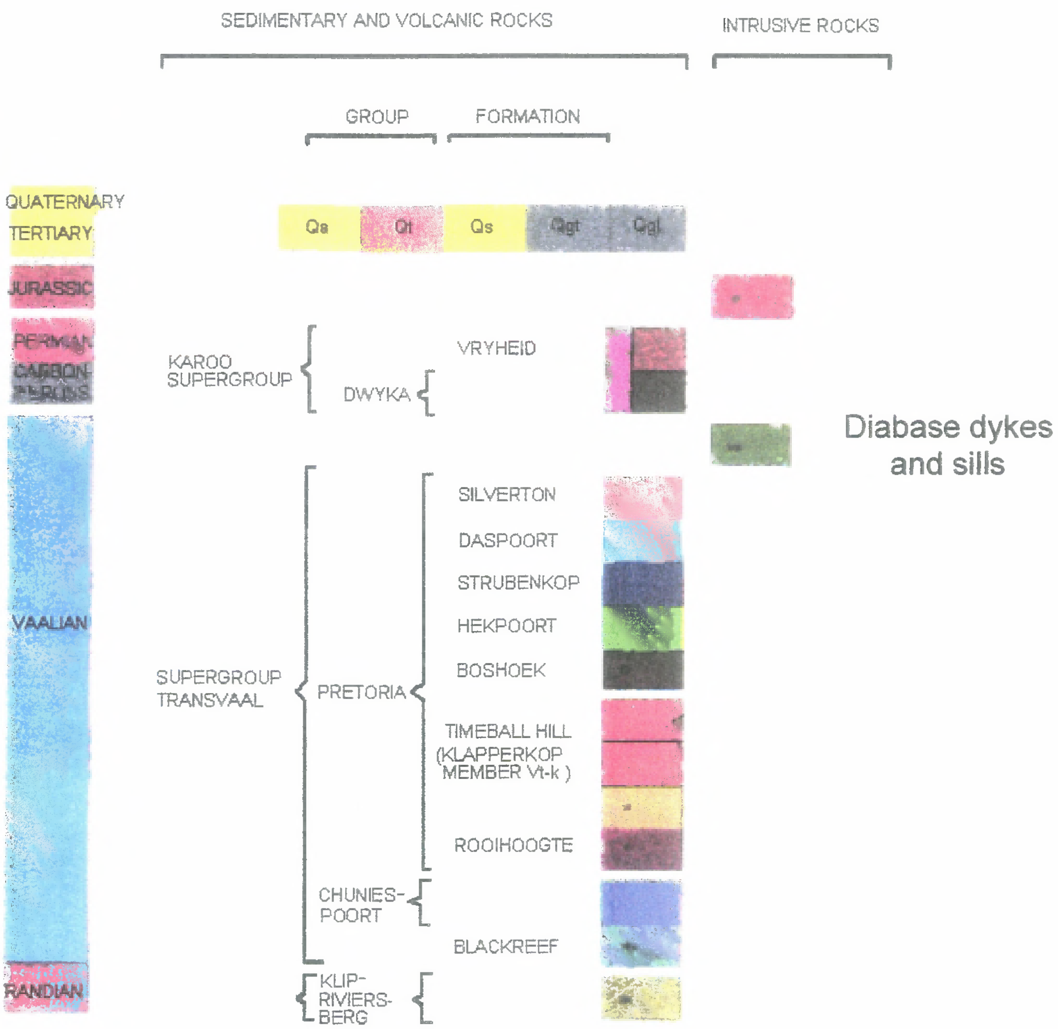

Figure 3(c) Stratigraphic sequence for 2627DB Vereeniging.

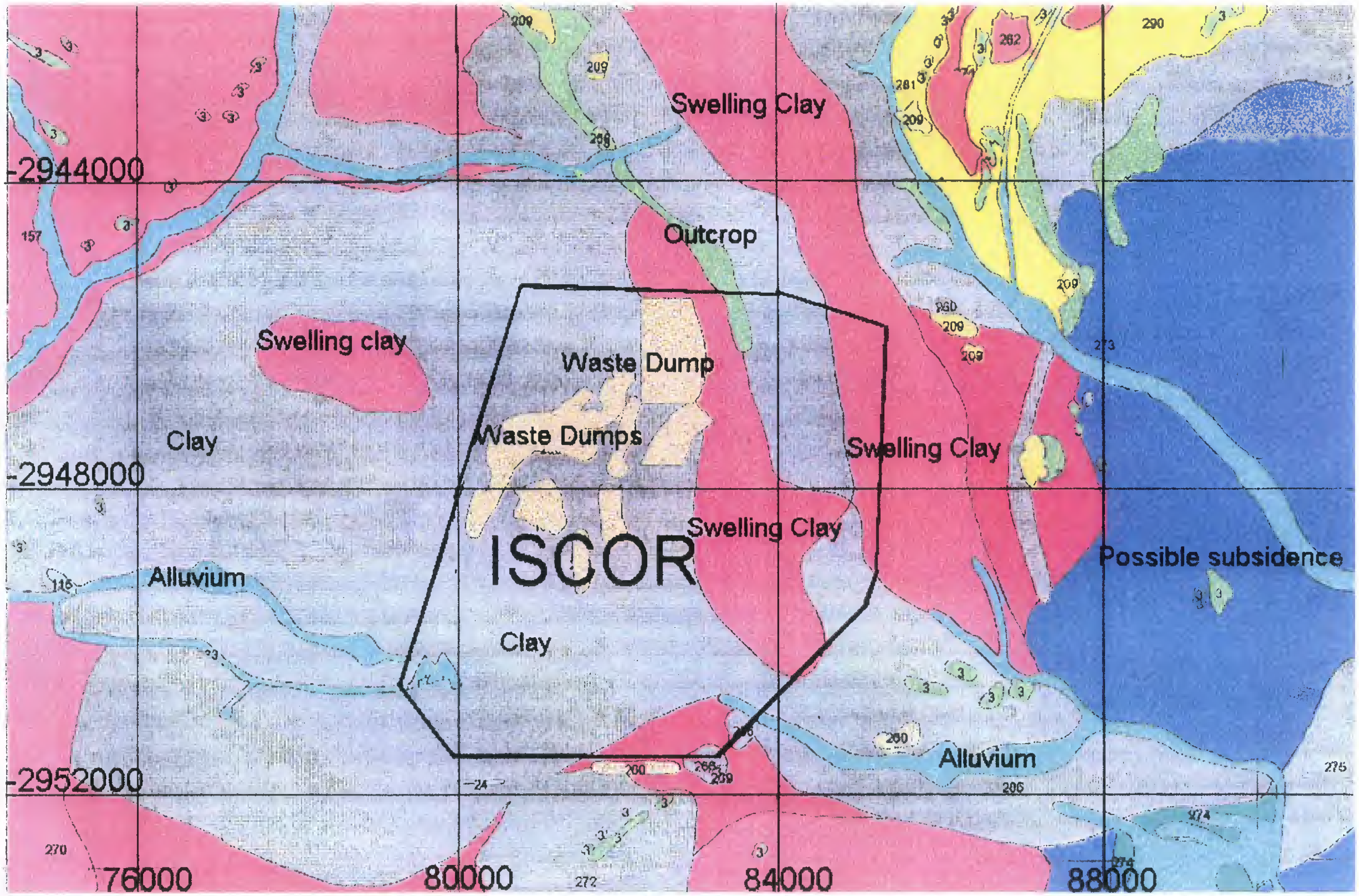

Figure 4. Classification of outcropping rock and soil material in the investigated area in terms of geotechnical parameters.

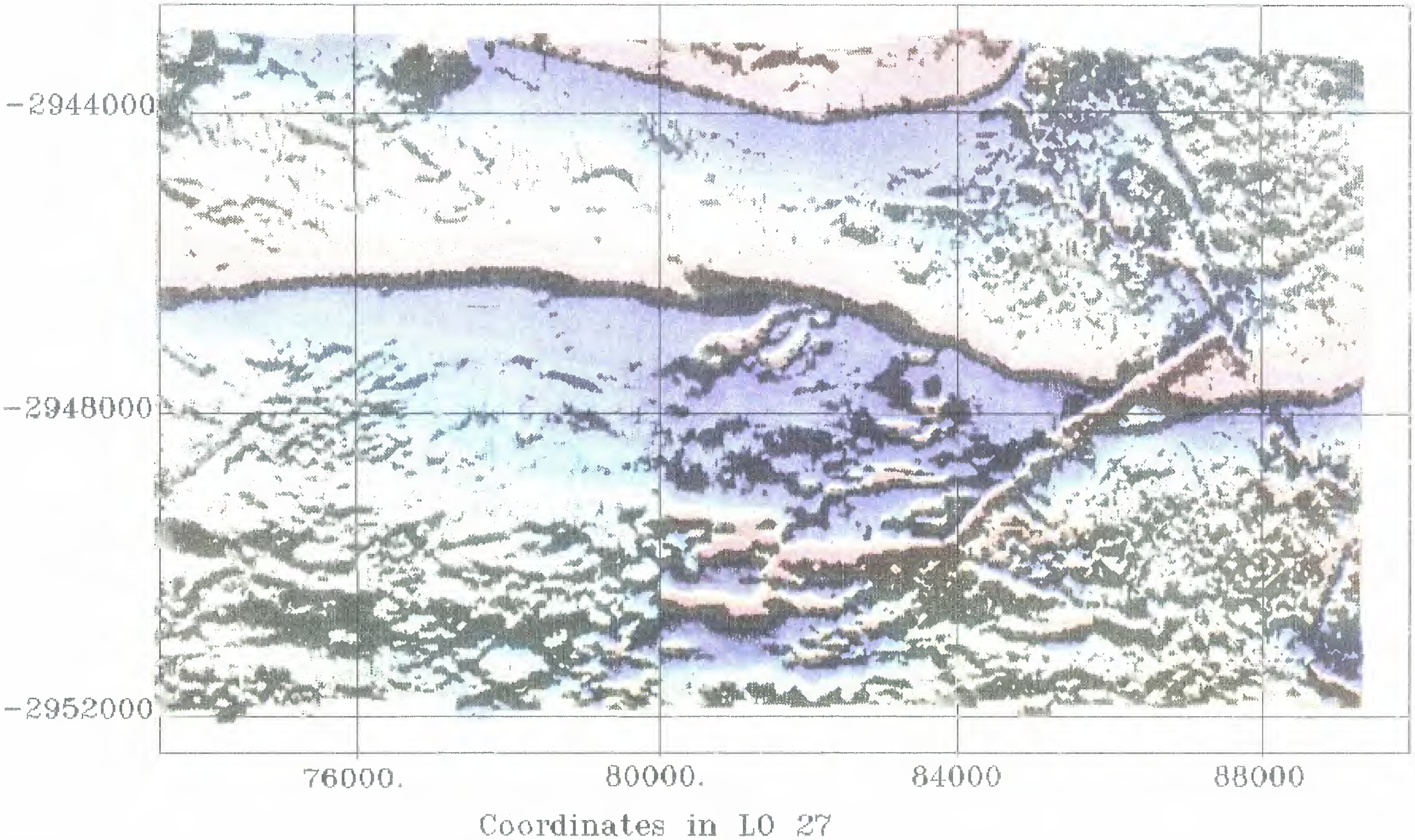

Figure 5. Total field aeromagnetic map with artificial sun shading from the north. Warm colours signify magnetic highs.

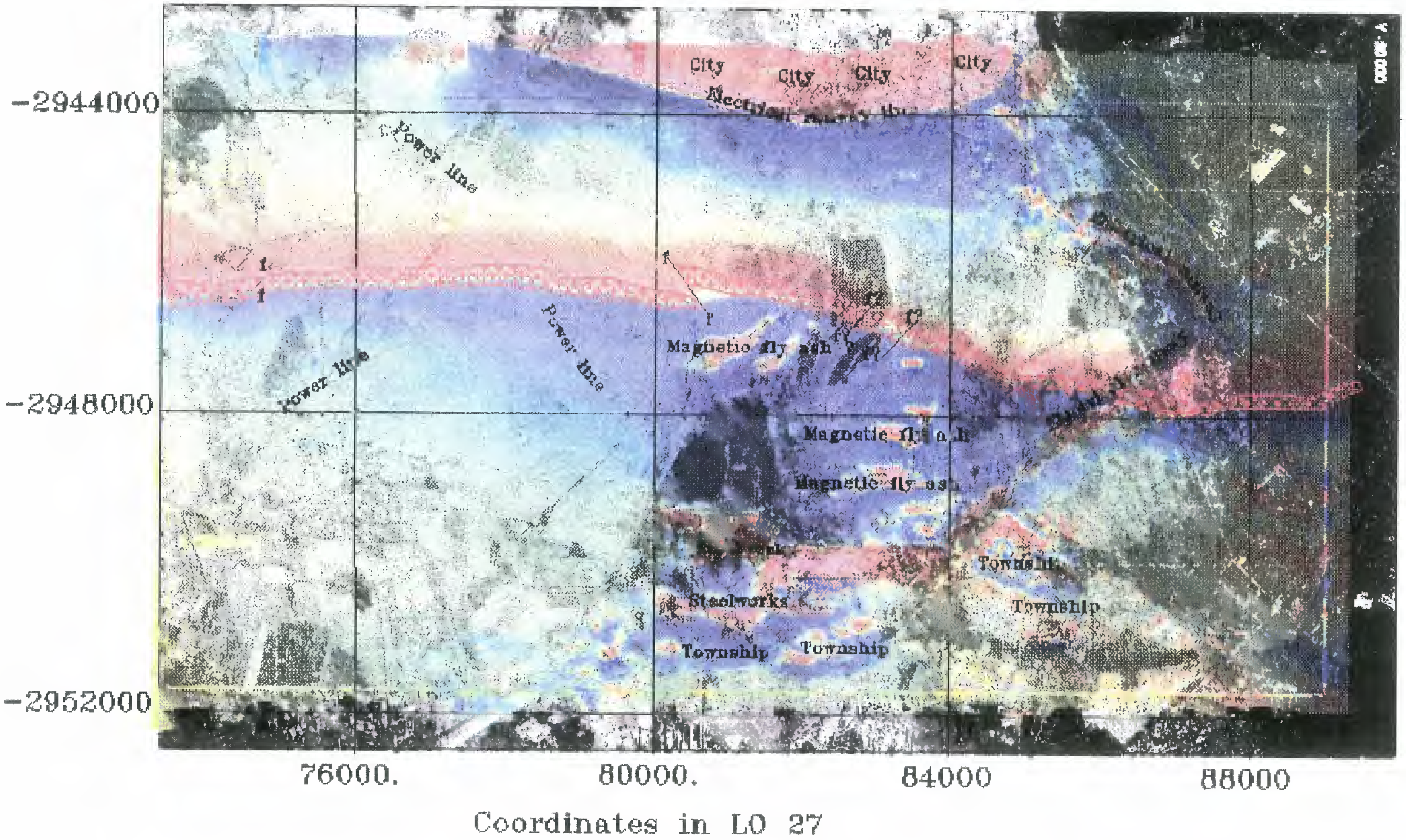

Figure 6. Qualitative interpretation of the magnetic data.

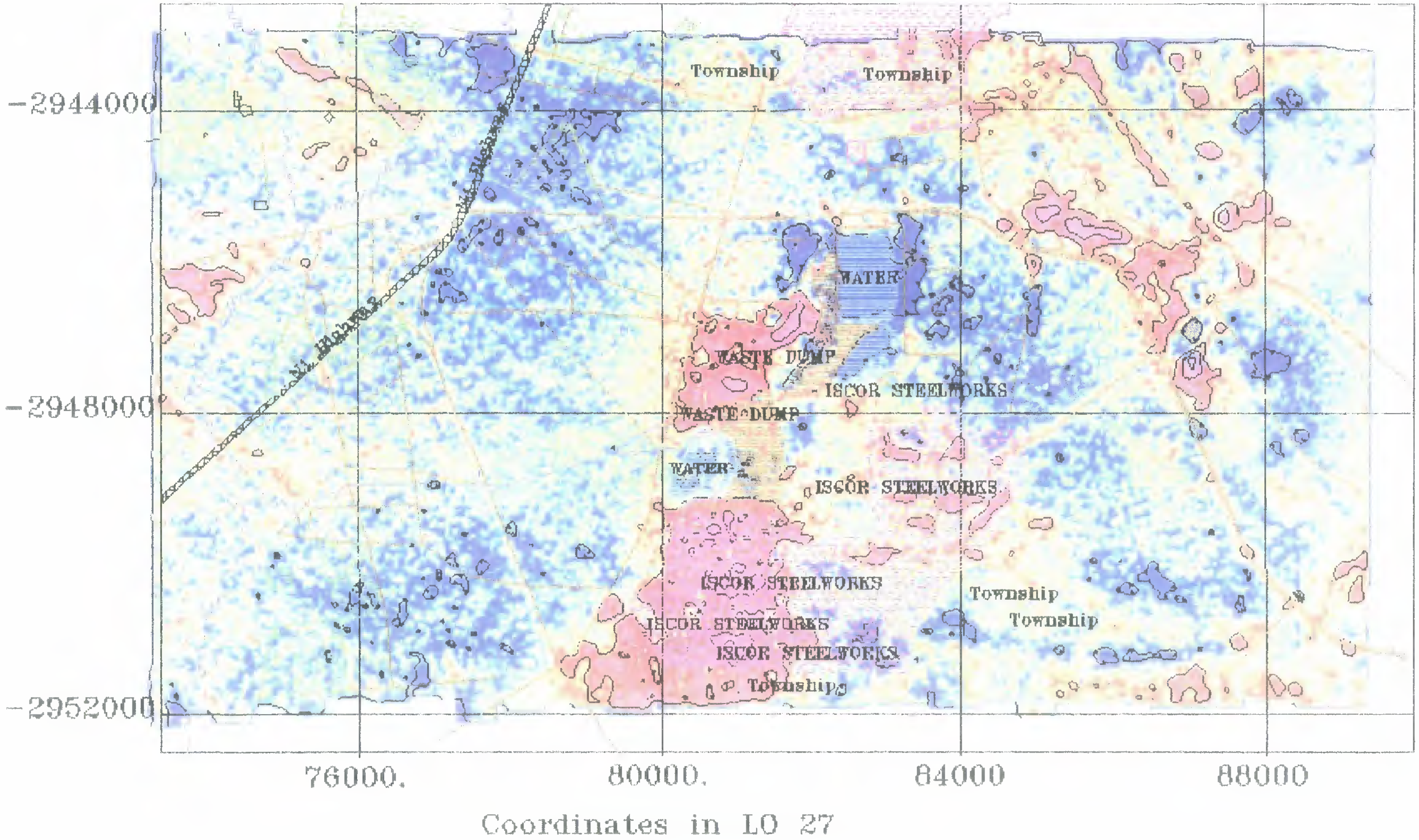

Figure 7. Colour coded Potassium concentration map. The maximum concentration is 8 per cent signified by the areas coloured deep red.

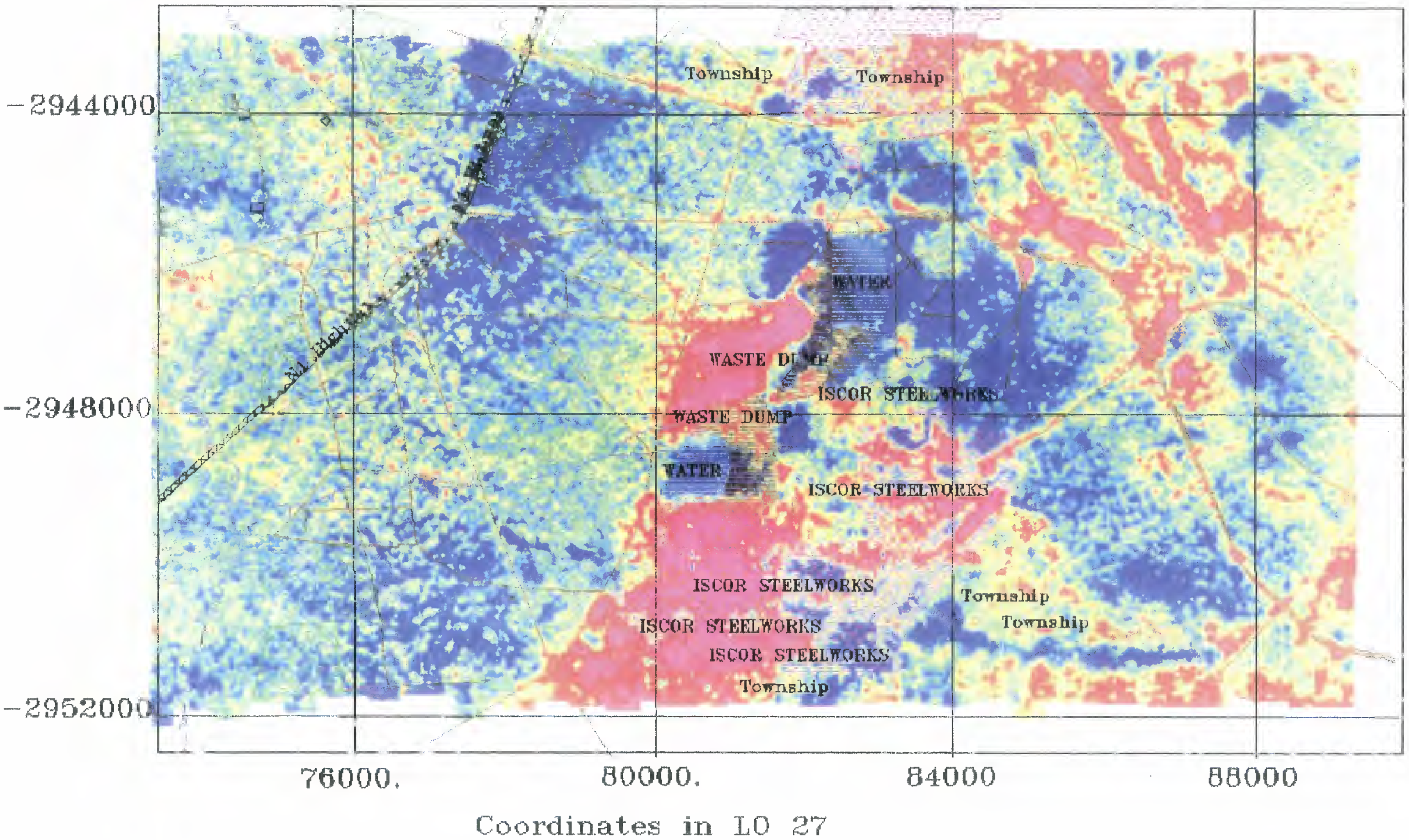

Figure 8. Colour coded Uranium concentration map in ppm. The highest concentration is 21ppm and occurs over the slag dumps, the steelworks and Vanderbijl Park. Maximum concentrations coloured dark red.

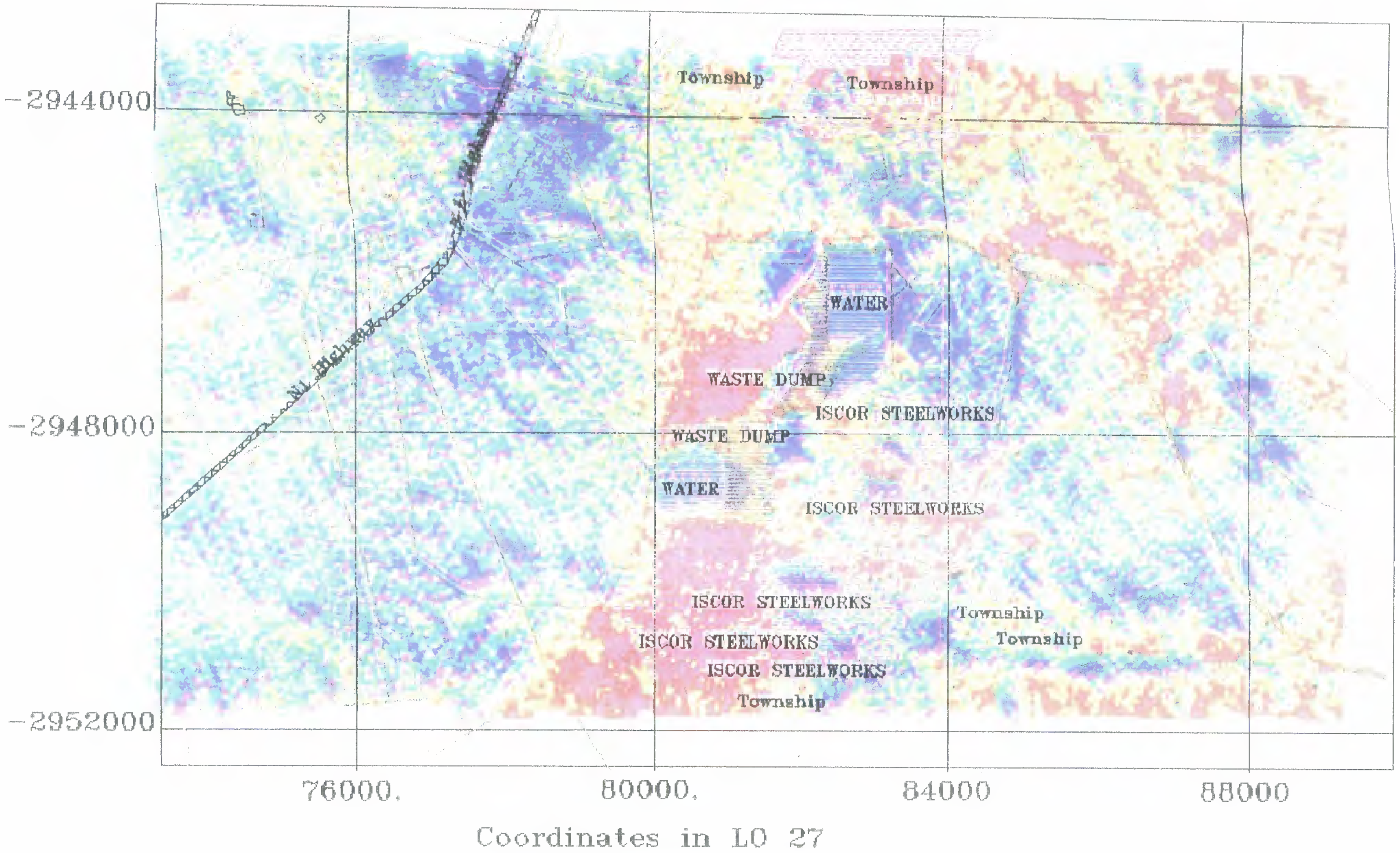

Figure 9. Colour coded Thorium concentration map in ppm. Highest concentration is 38ppm and occurs over the slag dumps, the steelworks and Vanderbijl Park.

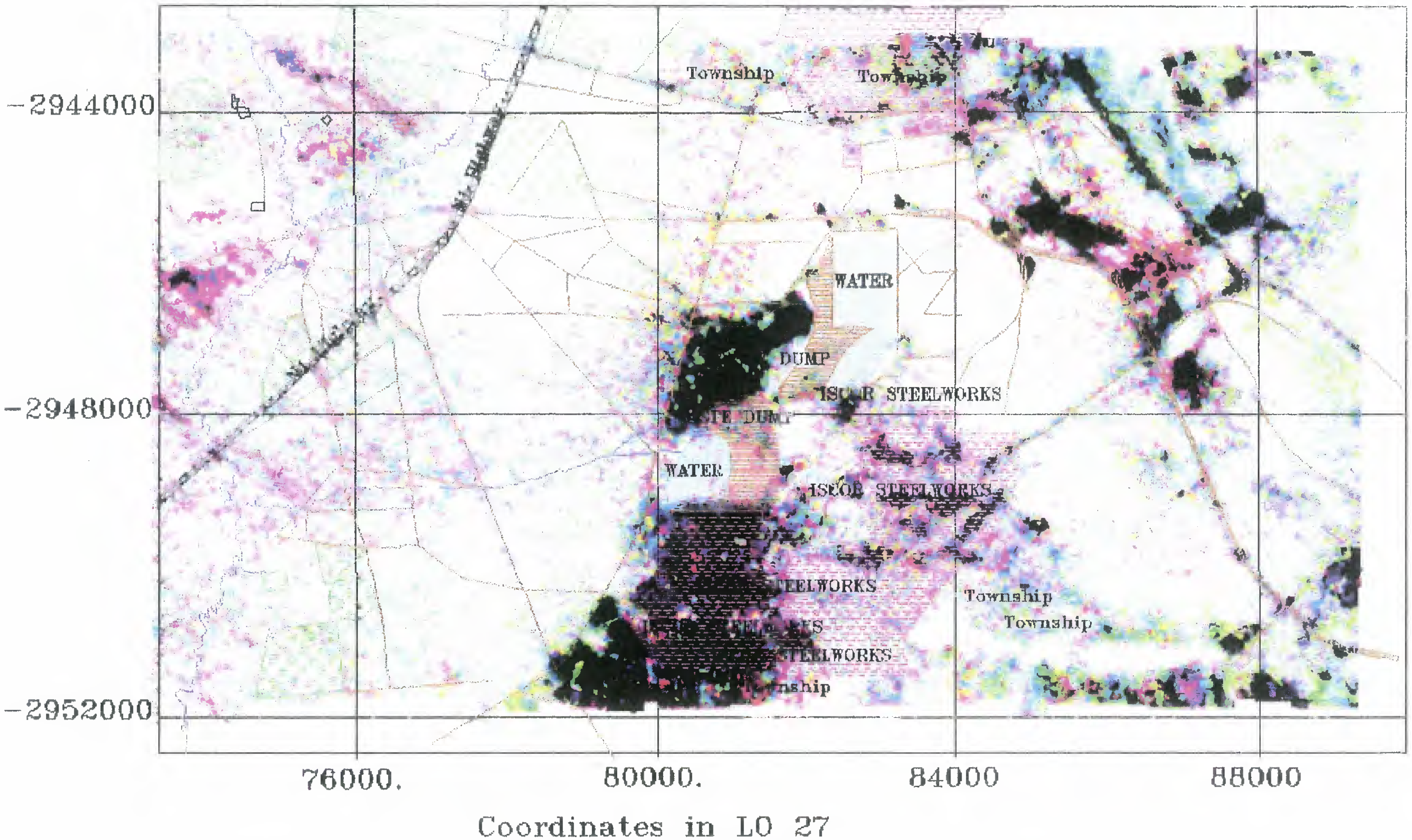

Figure 11. Ternary plot with magenta, cyan and yellow representing K, U and Th respectively.

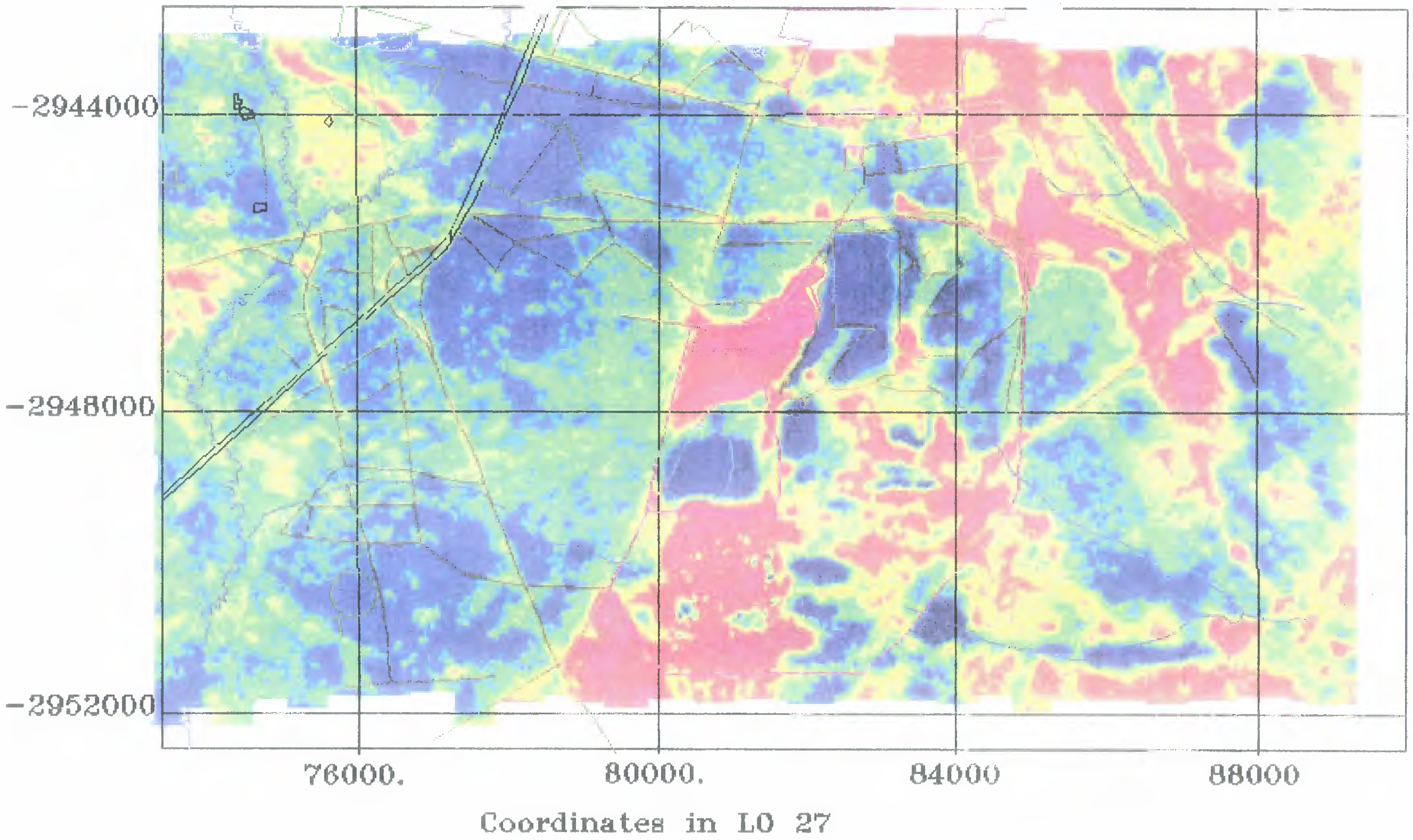

Figure 10. Colour coded gamma-ray Total Count map. The map summarises the contributions of all radiometric sources.

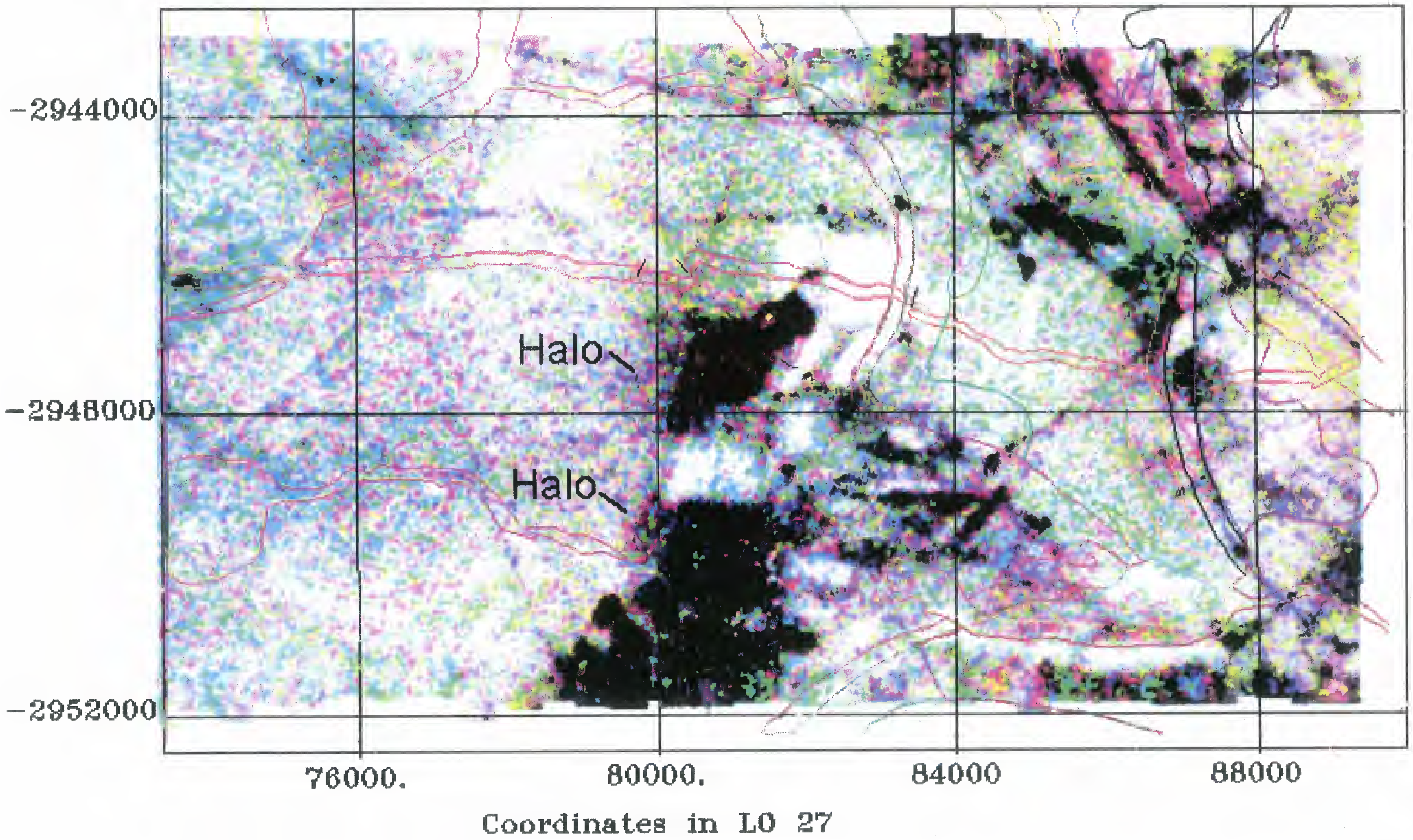

Figure 12. Radiometric ternary map with geology overlay.

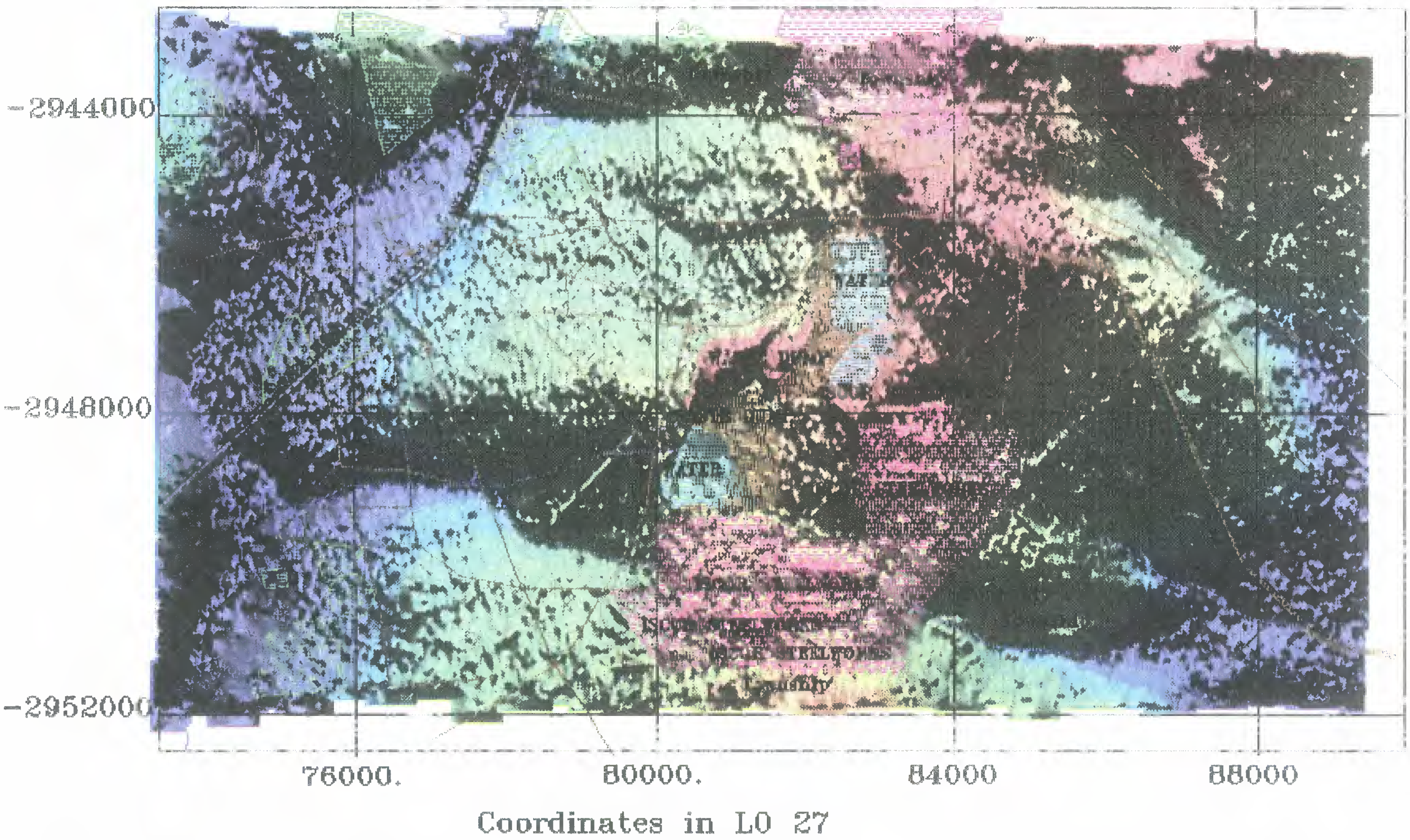

Figure 13. Digital terrain model as determined from the airborne geophysical survey. Infra structure map is overlain.

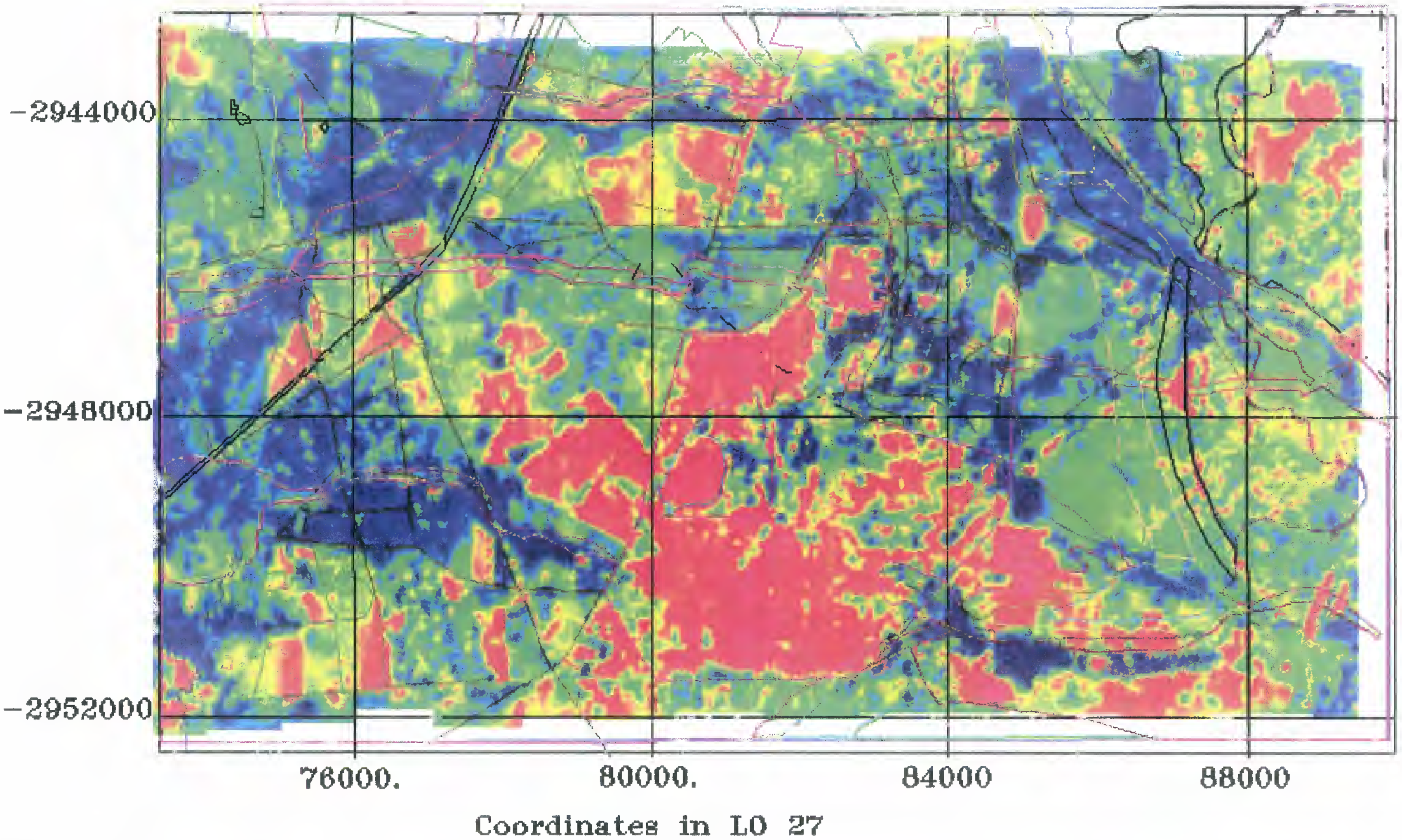

Figure 14. Representation of light absorption and emission for band 1 (1.0 to 1.2 micron) of the Near Infra Red (NIR) spectral Profiler. Geology outline is overlain.

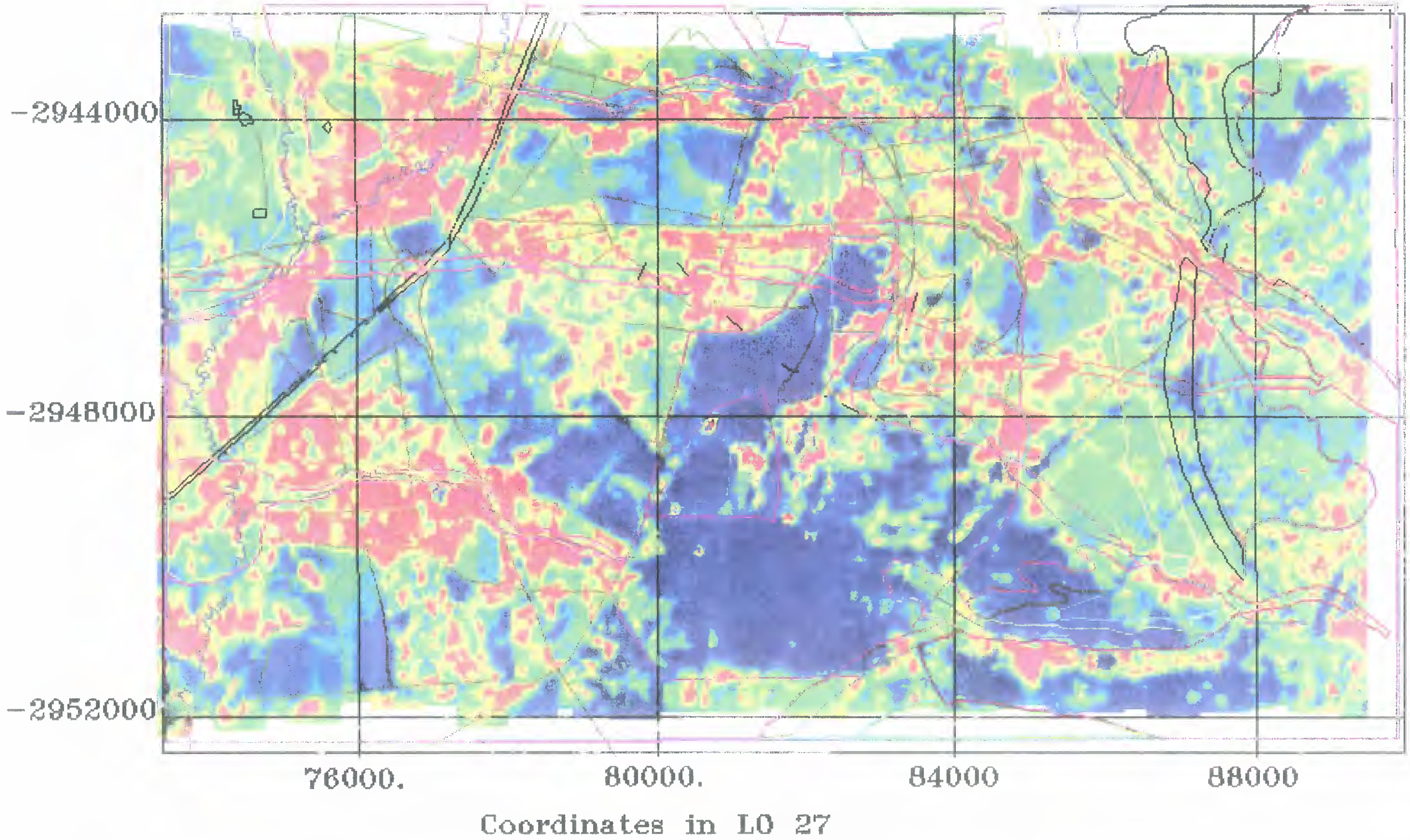

Figure 15. Representation of light absorption and emission for band 2 (1.2 to 1.4 micron) of the airborne Near Infra Red spectral profiler. Geology outline is overlain.

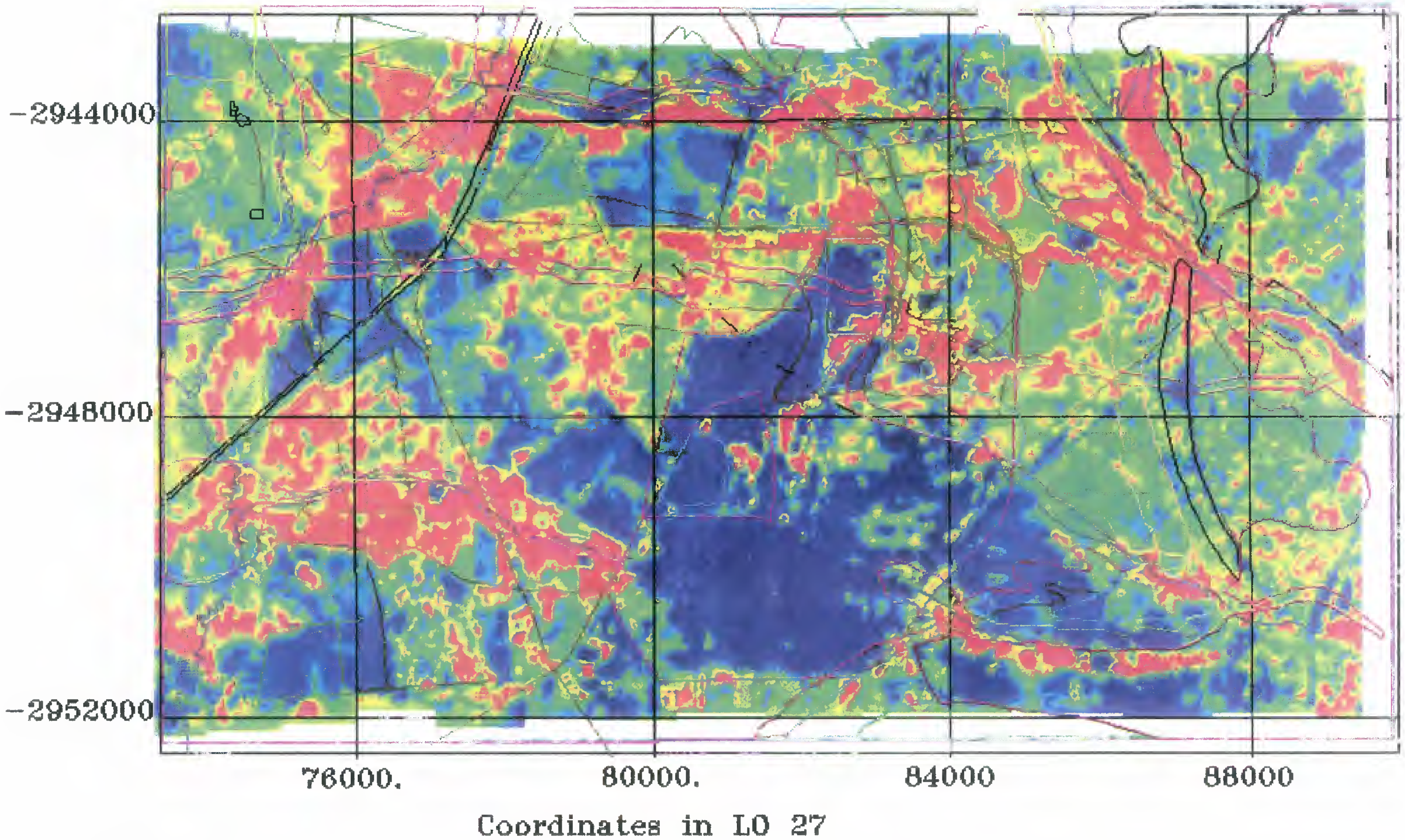

Figure 16. Representation of light absorption and emission for band 3 (1.4 to 1.6 micron) of the airborne Near Infra Red (NIR) spectral profiler. Geology outline is overlain.

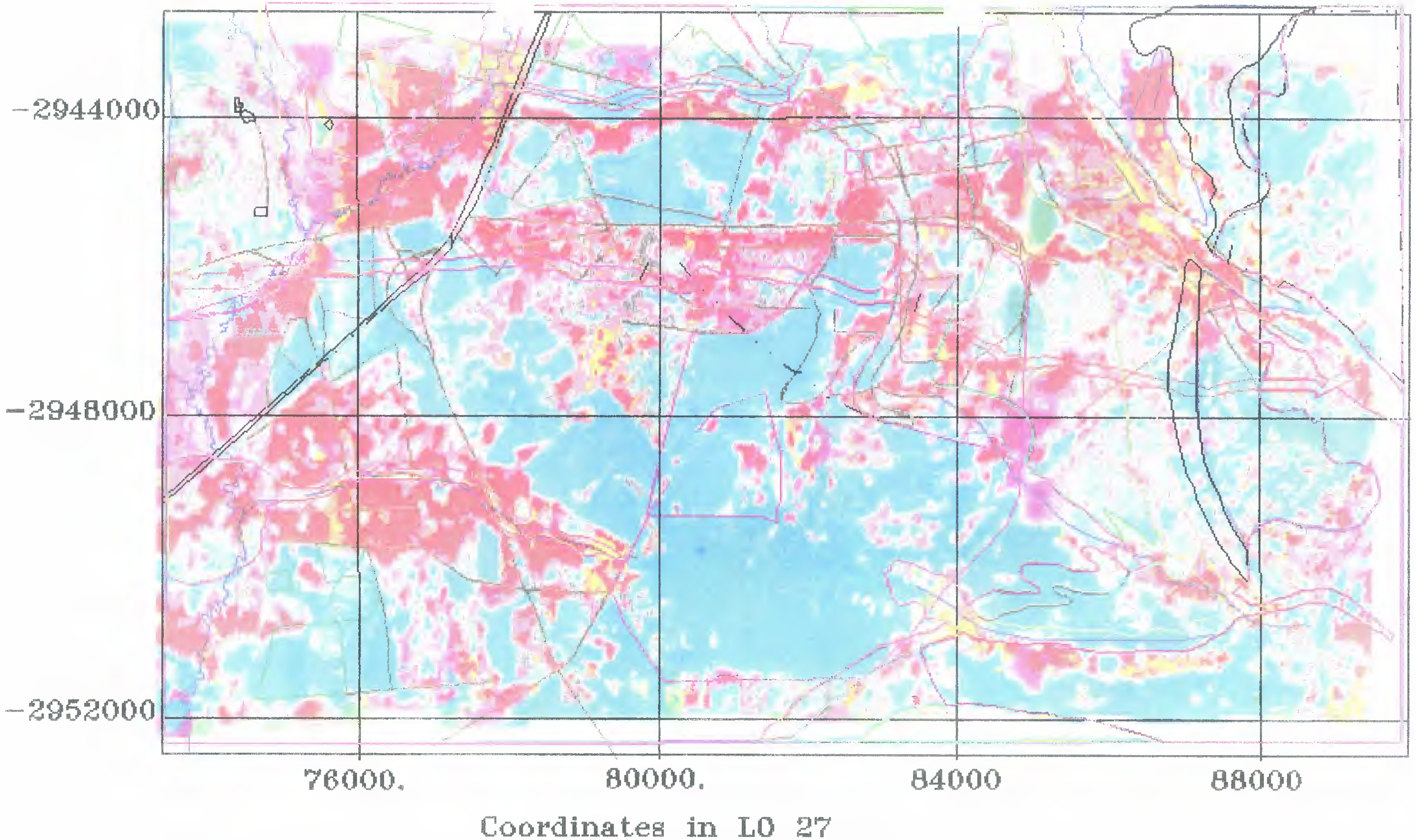

Figure 17. Ternary NIR image of bands 1, 2 and 3 for the area under investigation. The geology and infra structure maps are overlain.

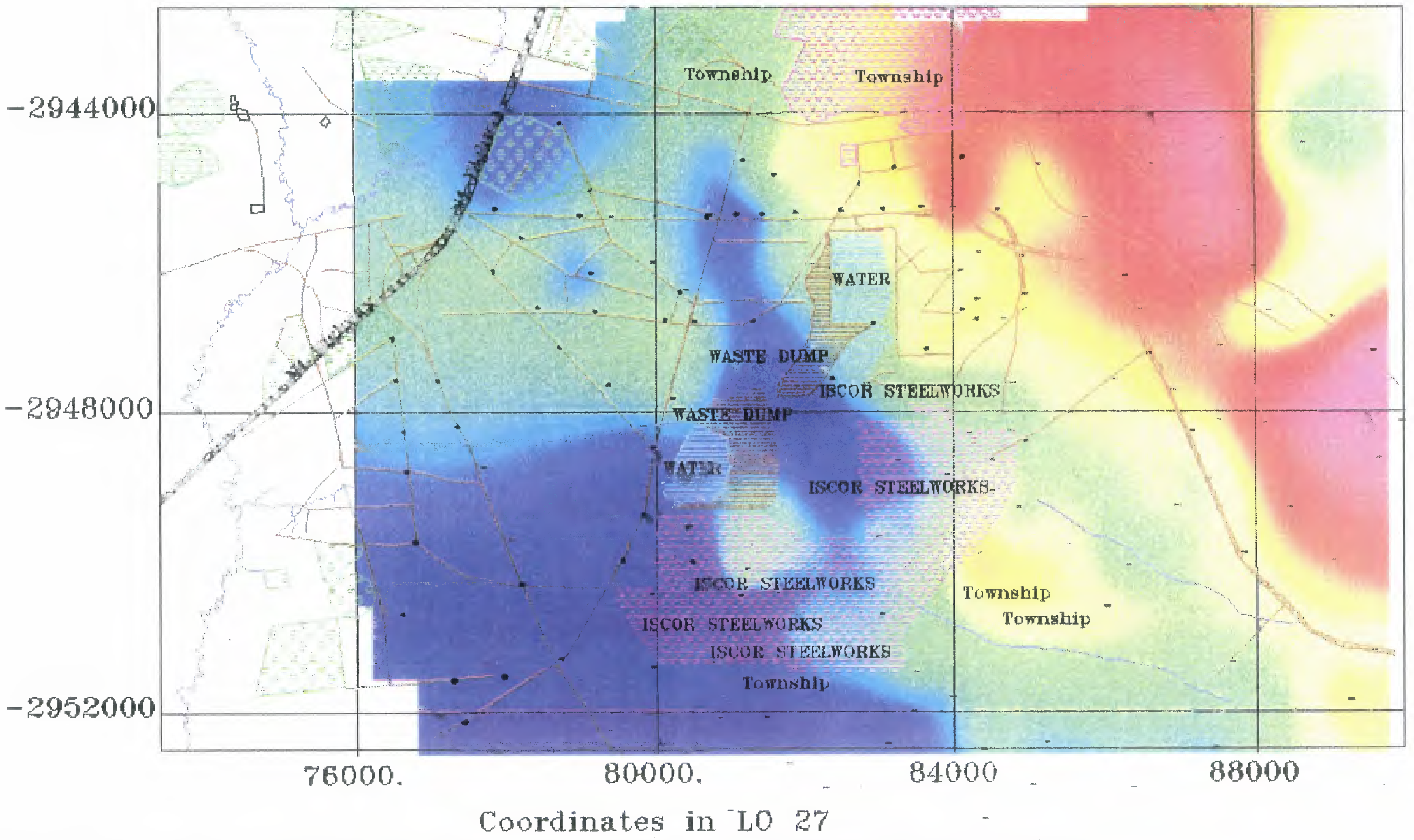

Figure 18. Distribution of gravity measurements in relation to the Steelworks and surroundings.

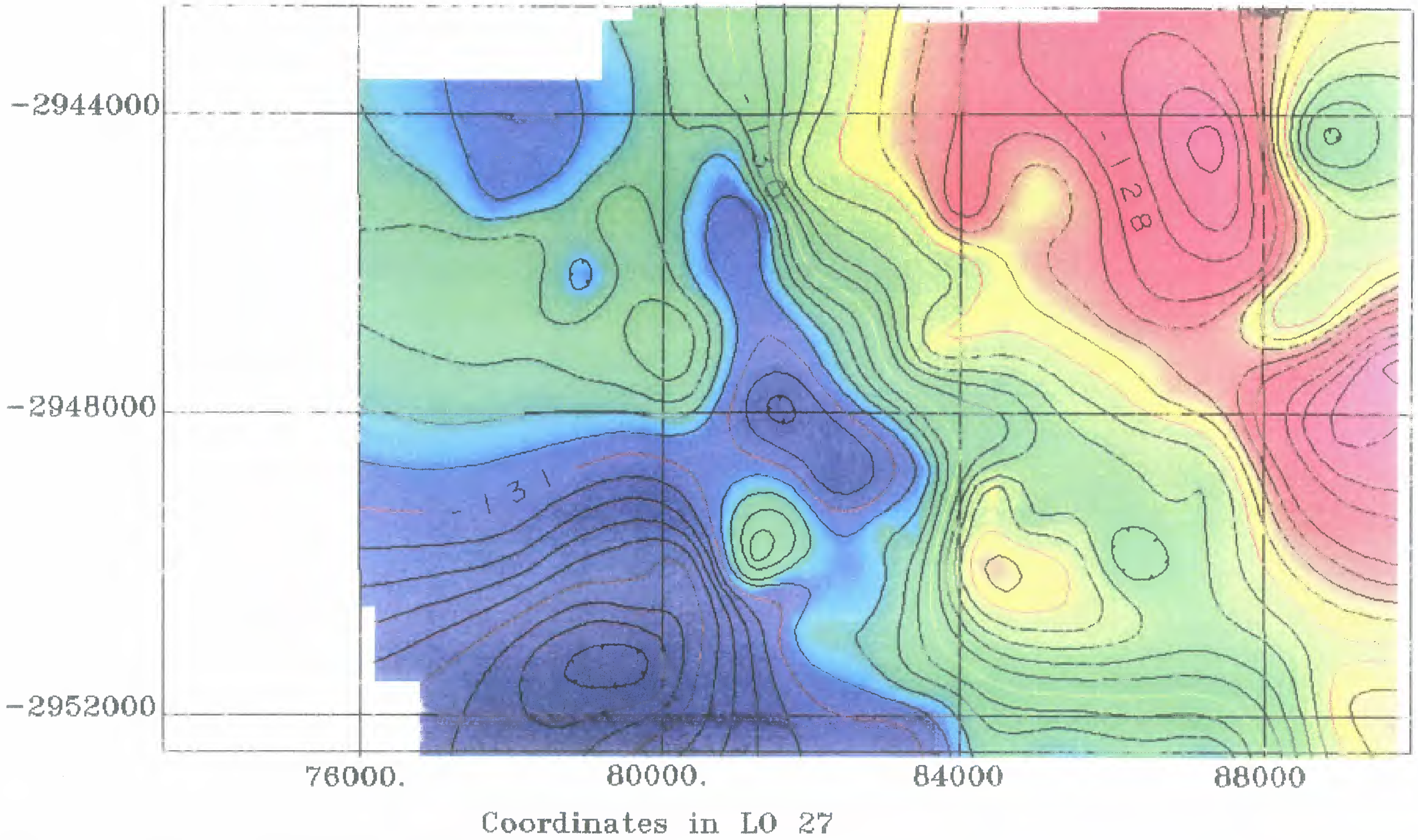

Figure 19. Colour coded Bouguer gravity contour map.

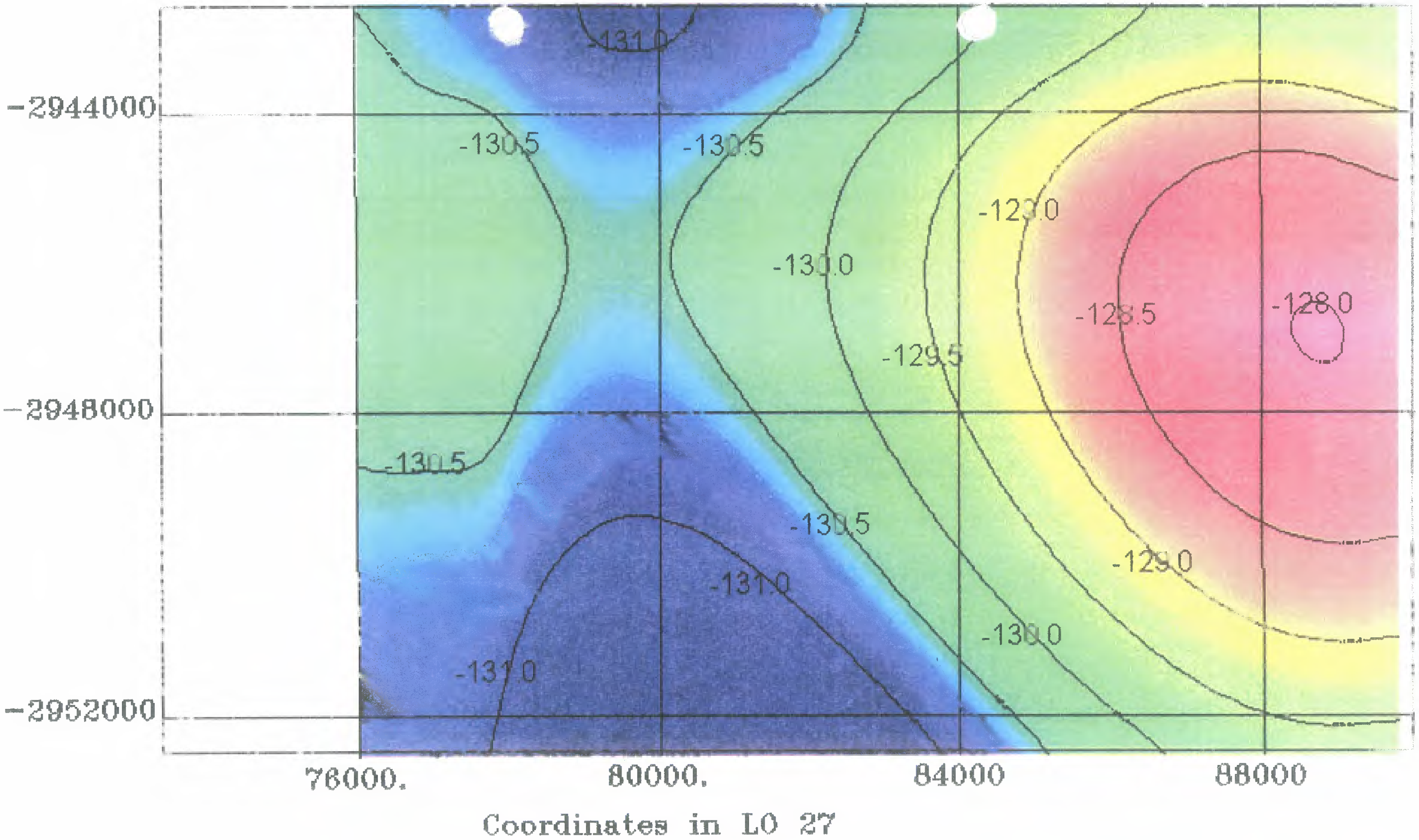

Figure 20. Regional field removed.

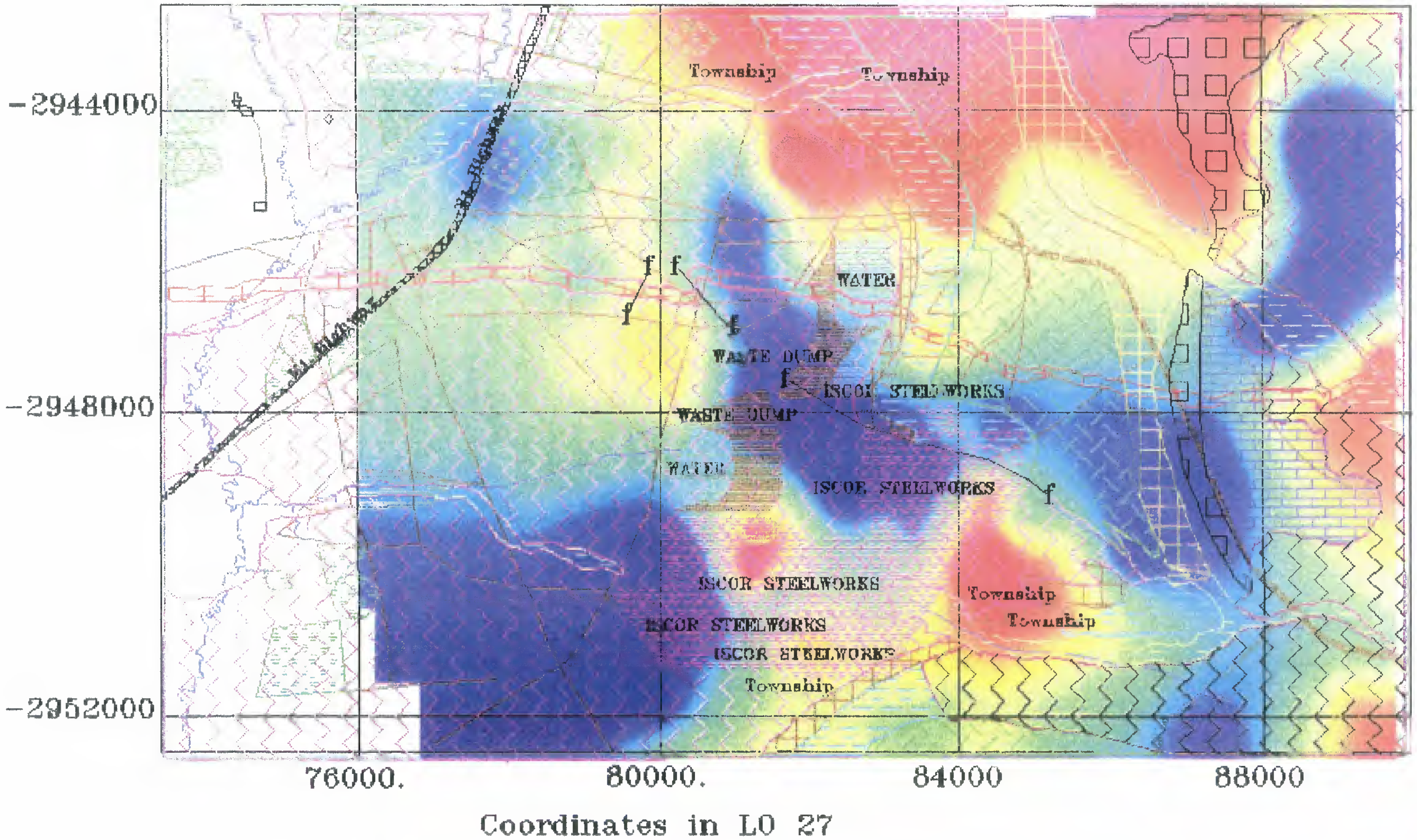

Figure 21. Residual gravity field superimposed on the geology and infrastructure.

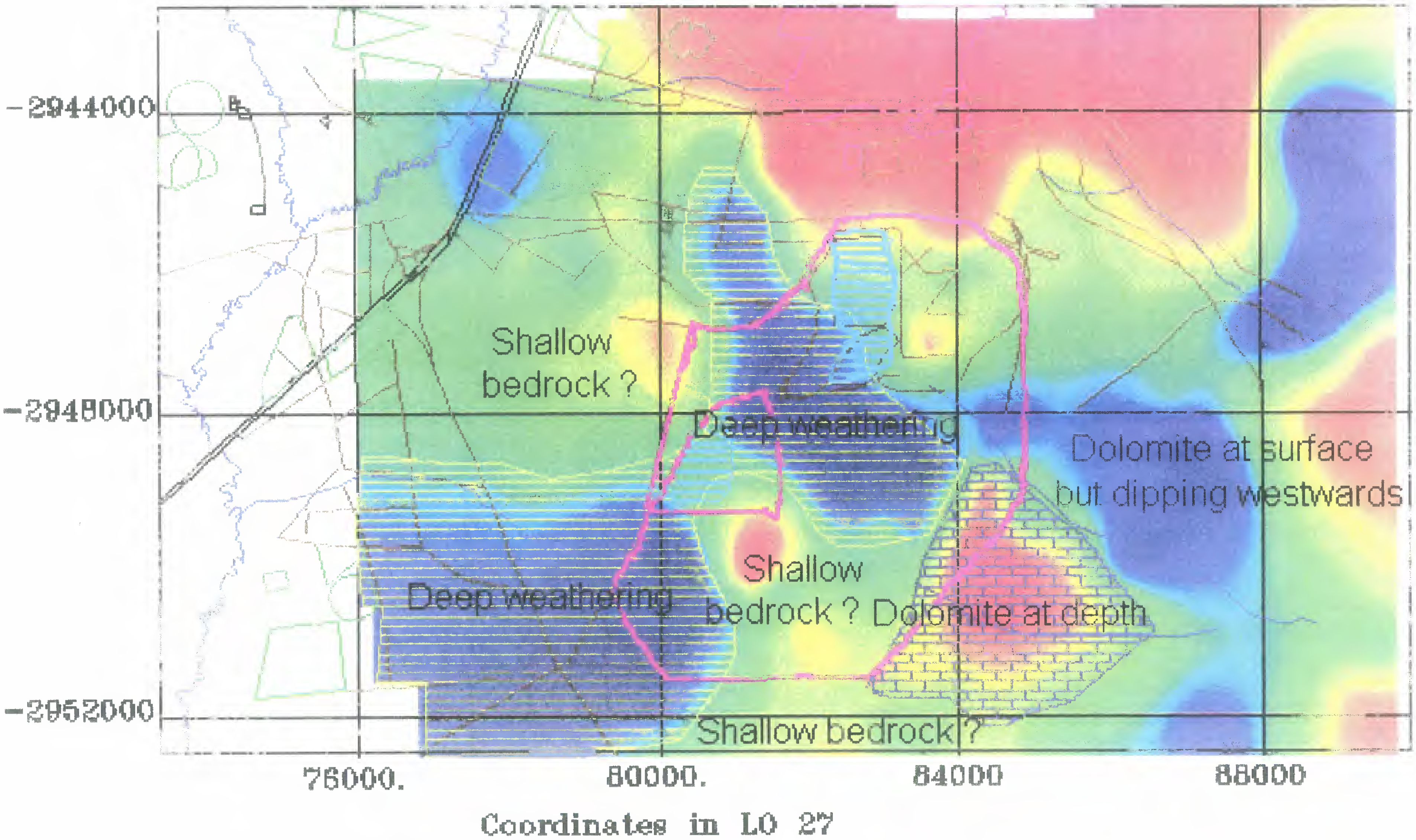

Figure 22. Qualitative interpretation of the residual gravity data.

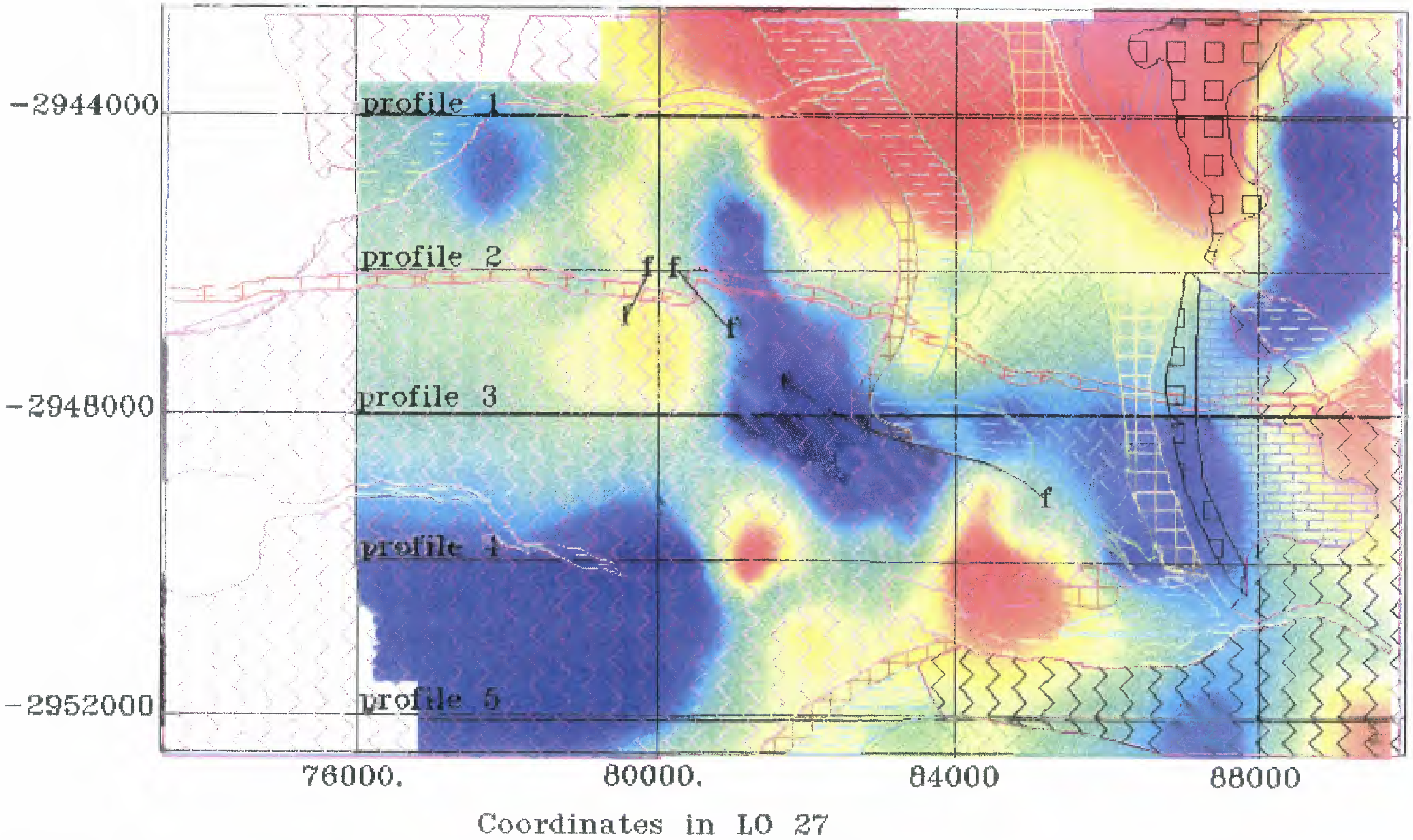

Figure 23. Profiles selected for quantitative interpretation in relation to the geology.

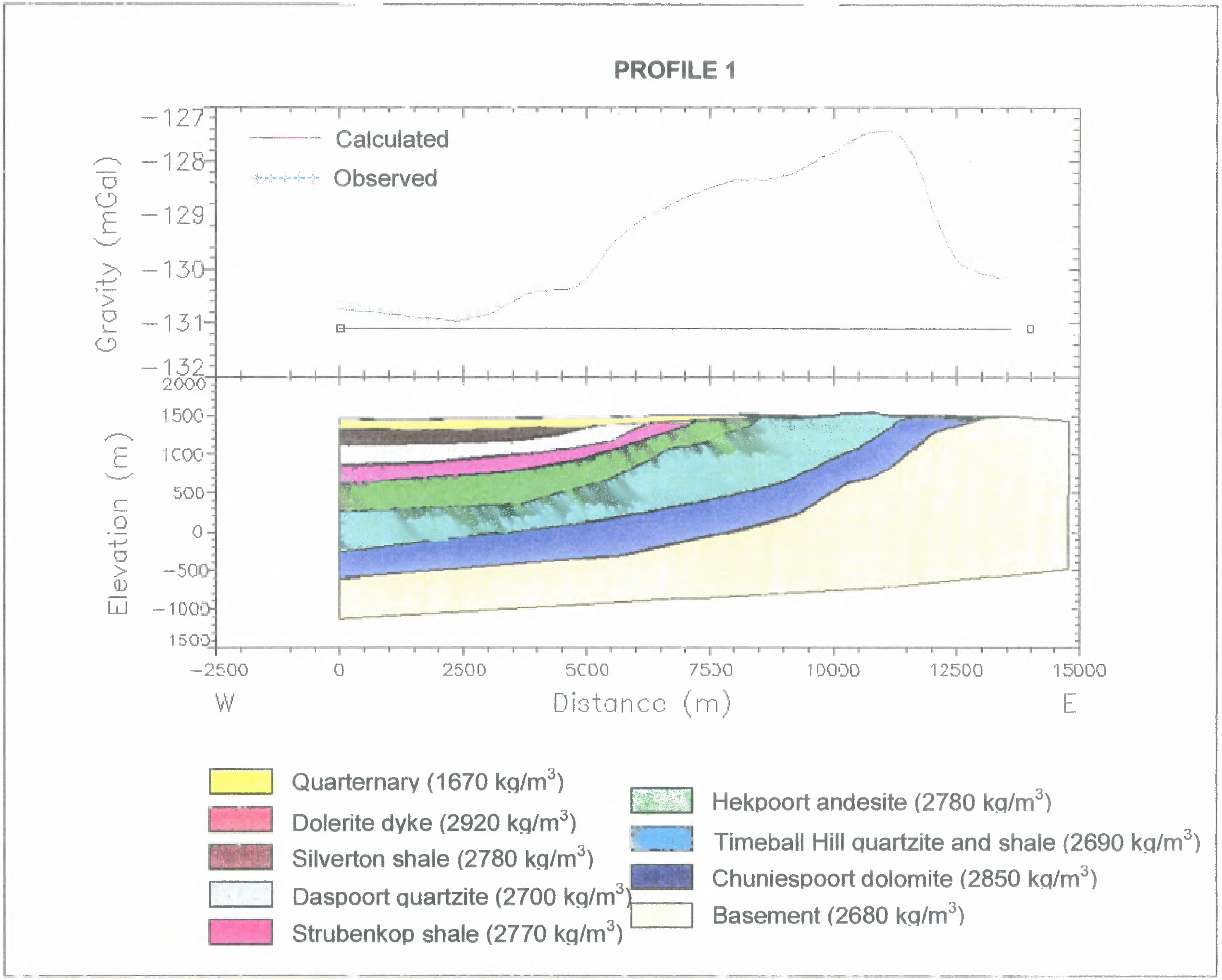

Figure 24. Model along profile A-A'

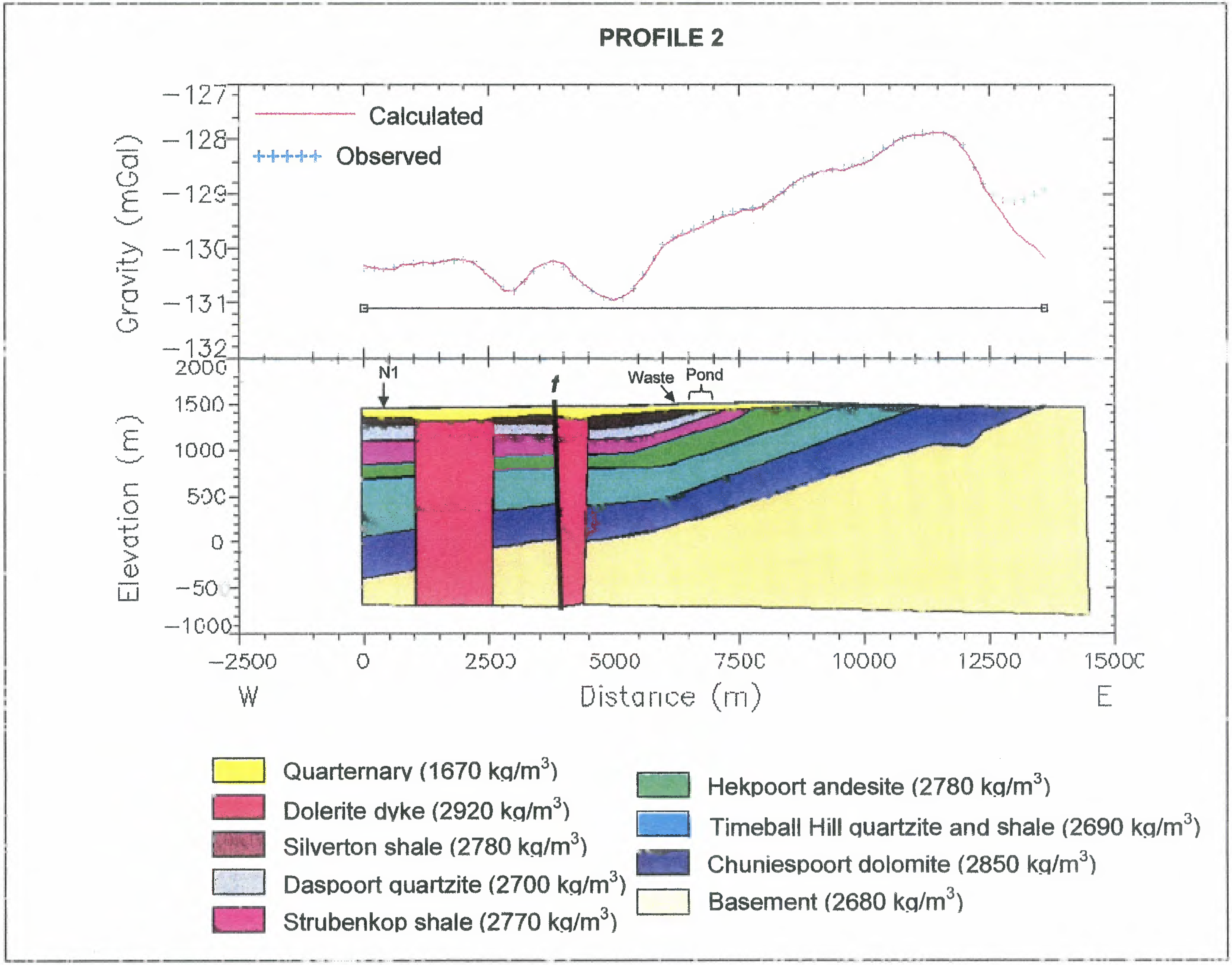

Figure 25. Model along profile B-B'

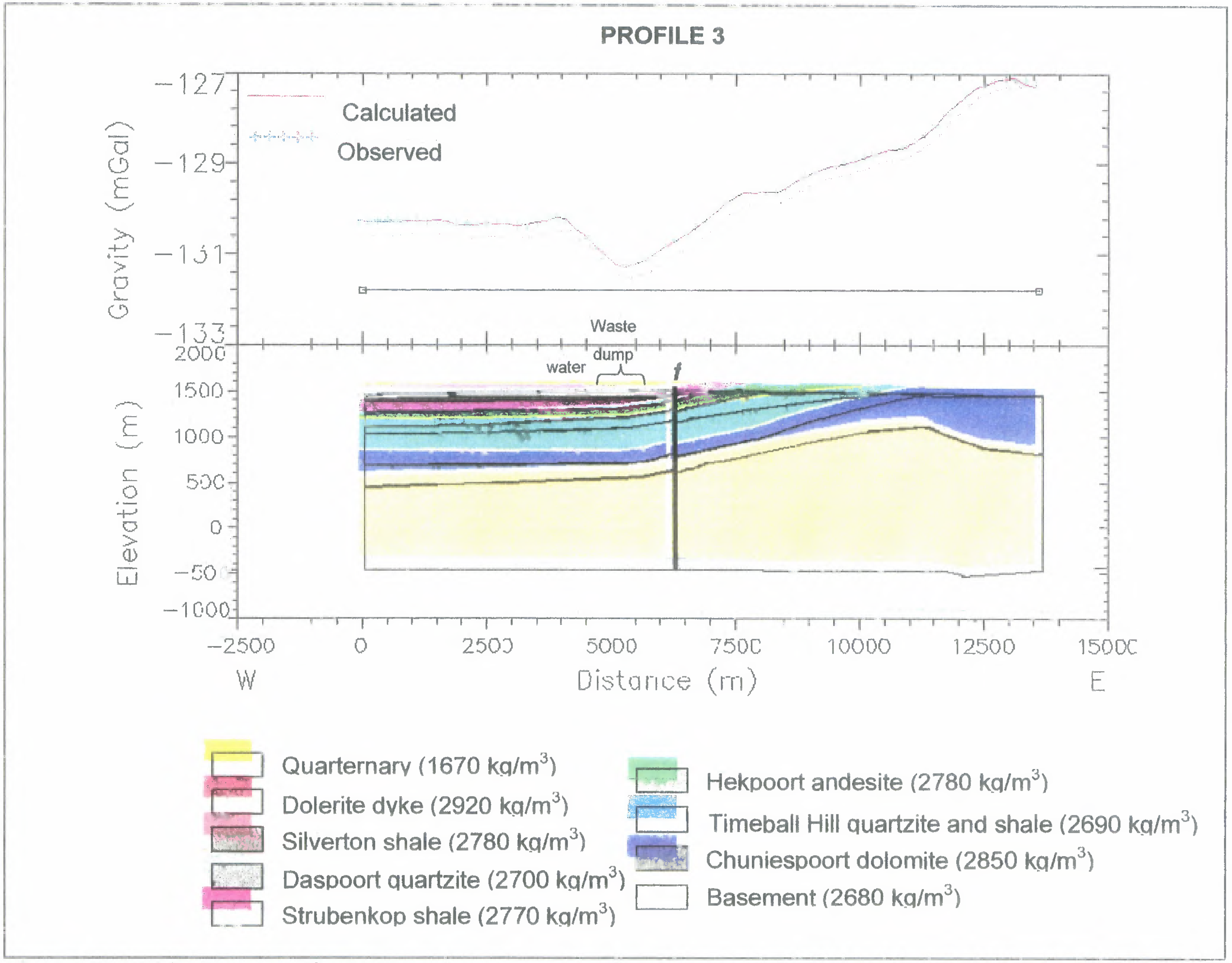

Figure 26. Model along profile C-C'

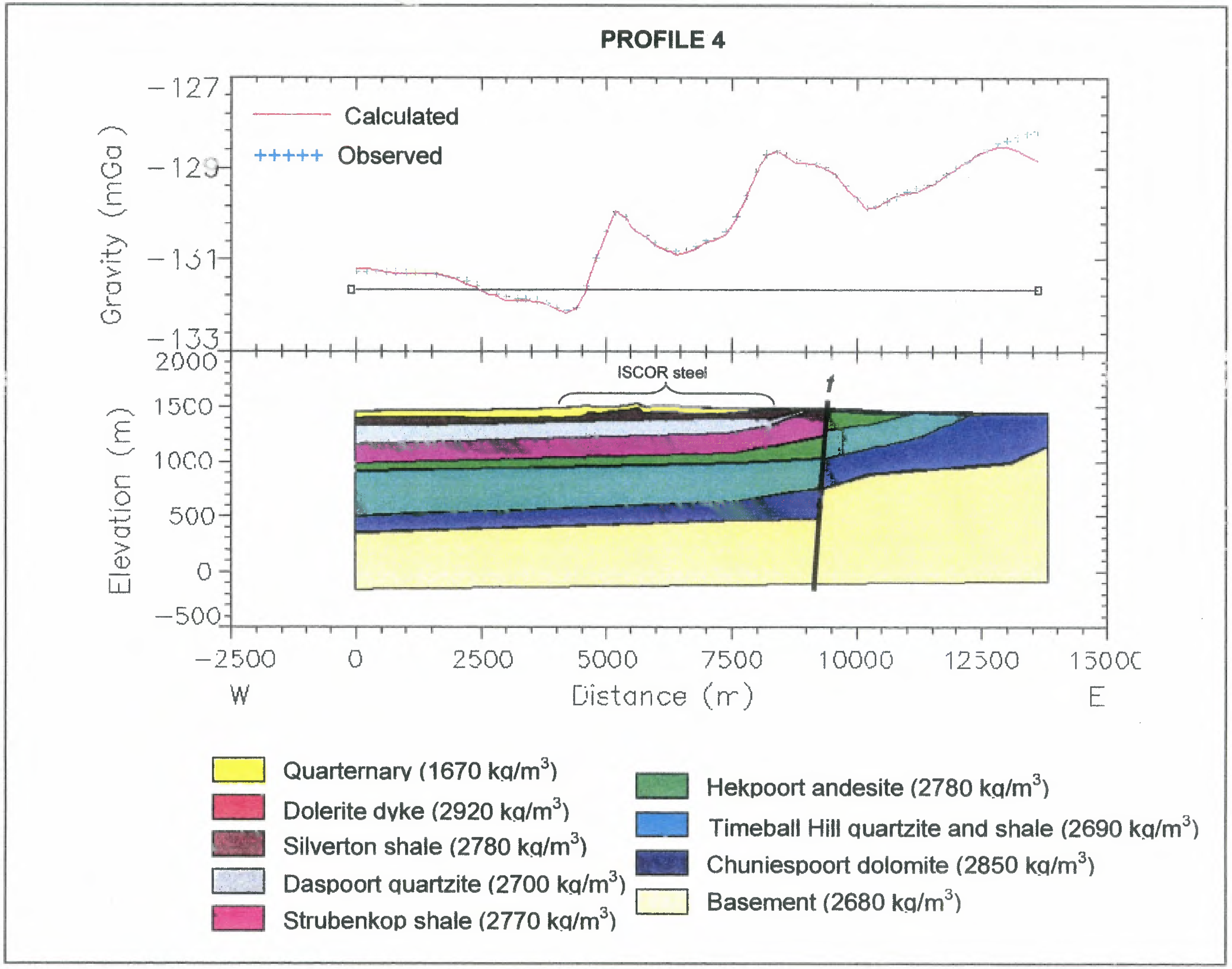

Figure 27. Model along profile D-D'

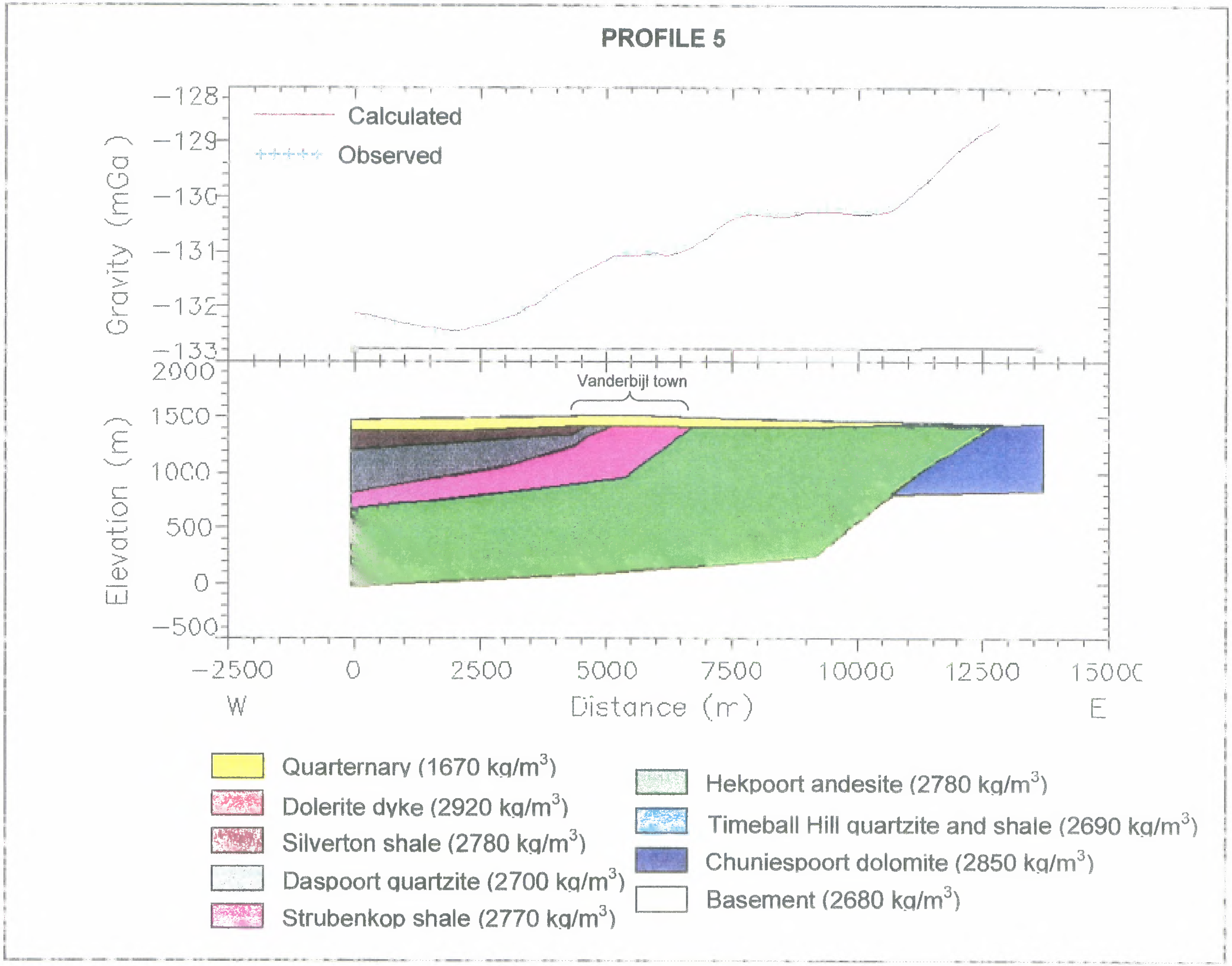

Figure 28. Model along profile E-E'

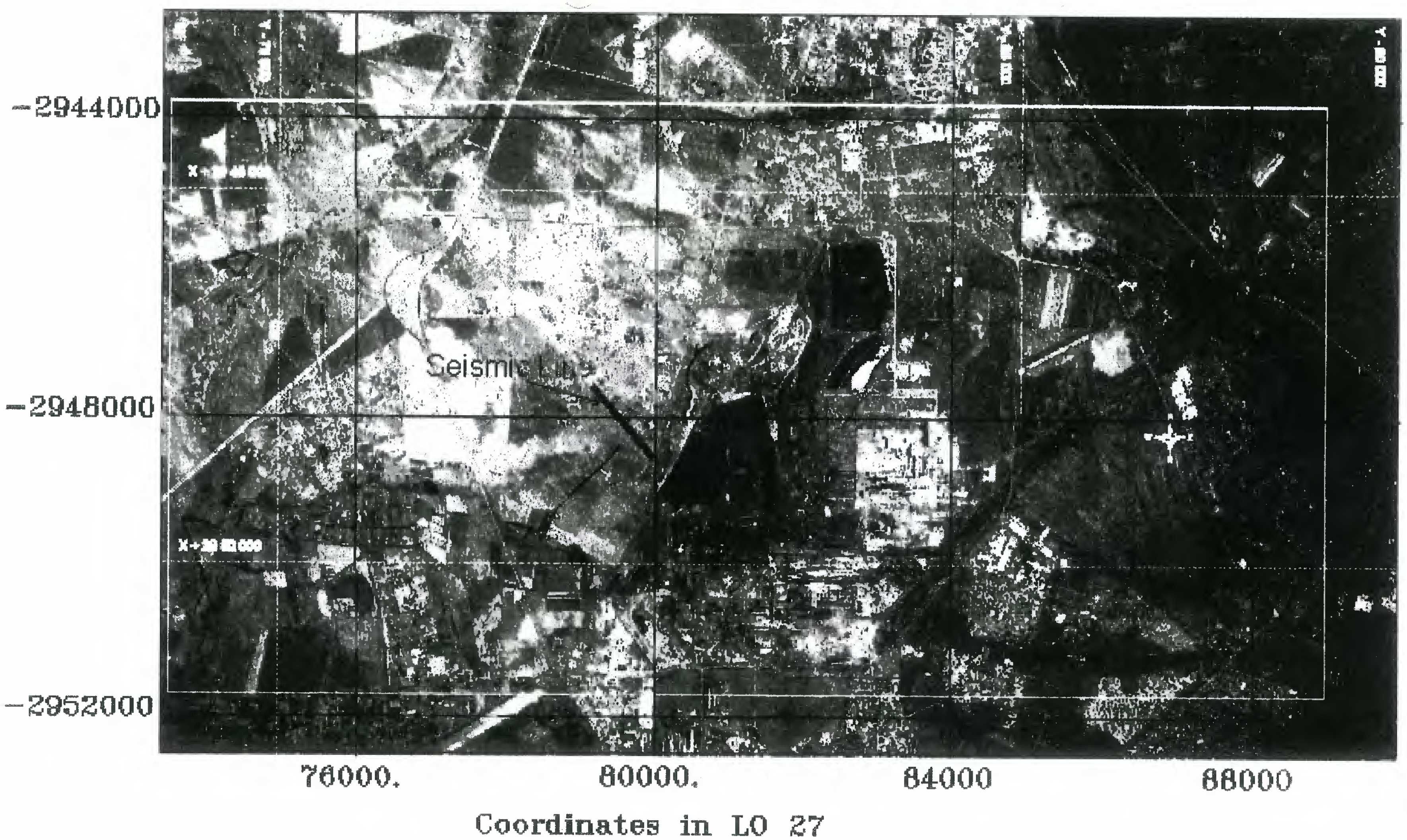

Figure 29. Location of the reflection seismic line in relation to the steelworks.

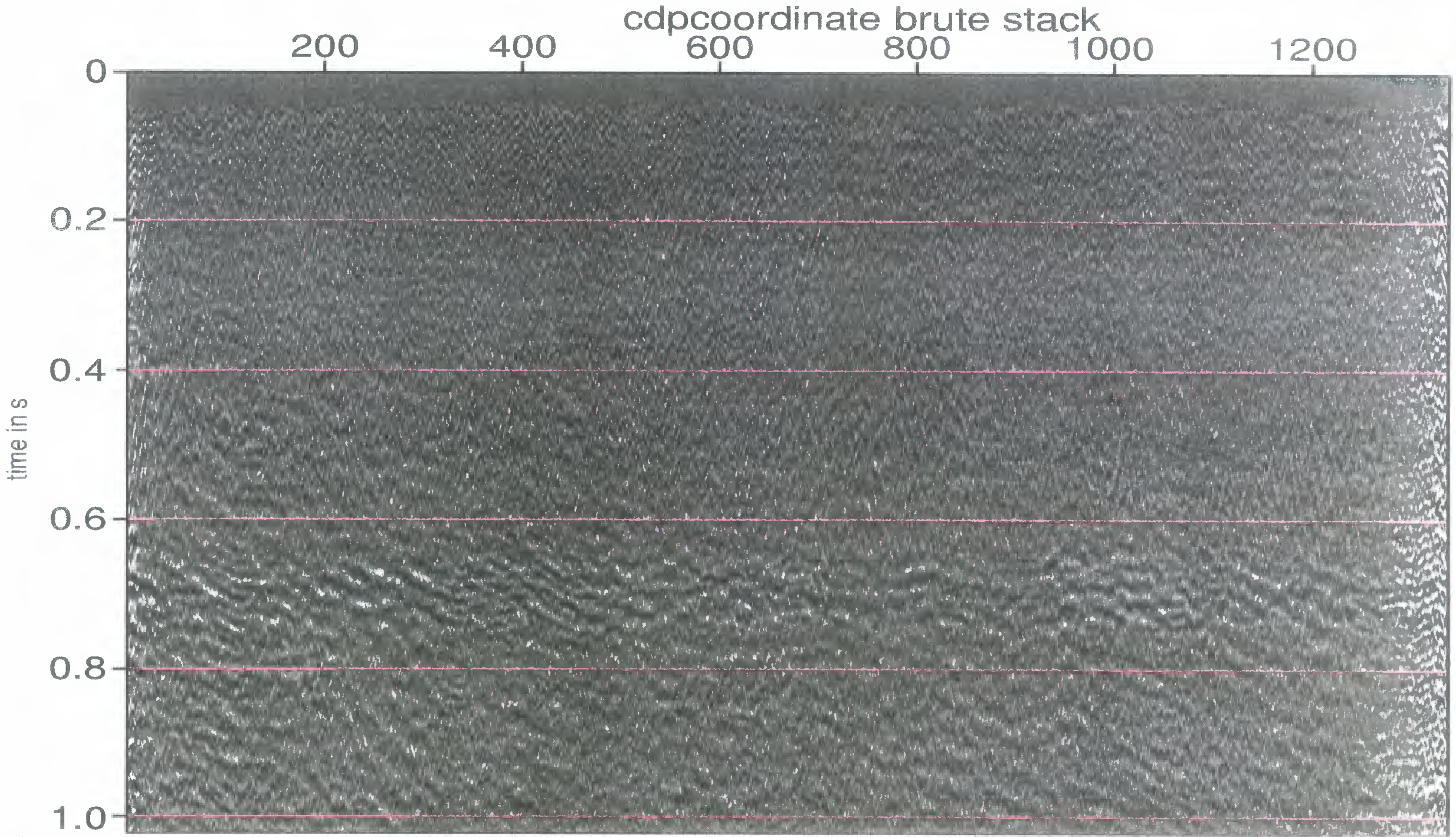

Figure 30. Brute stack of the reflection seismic data collected.

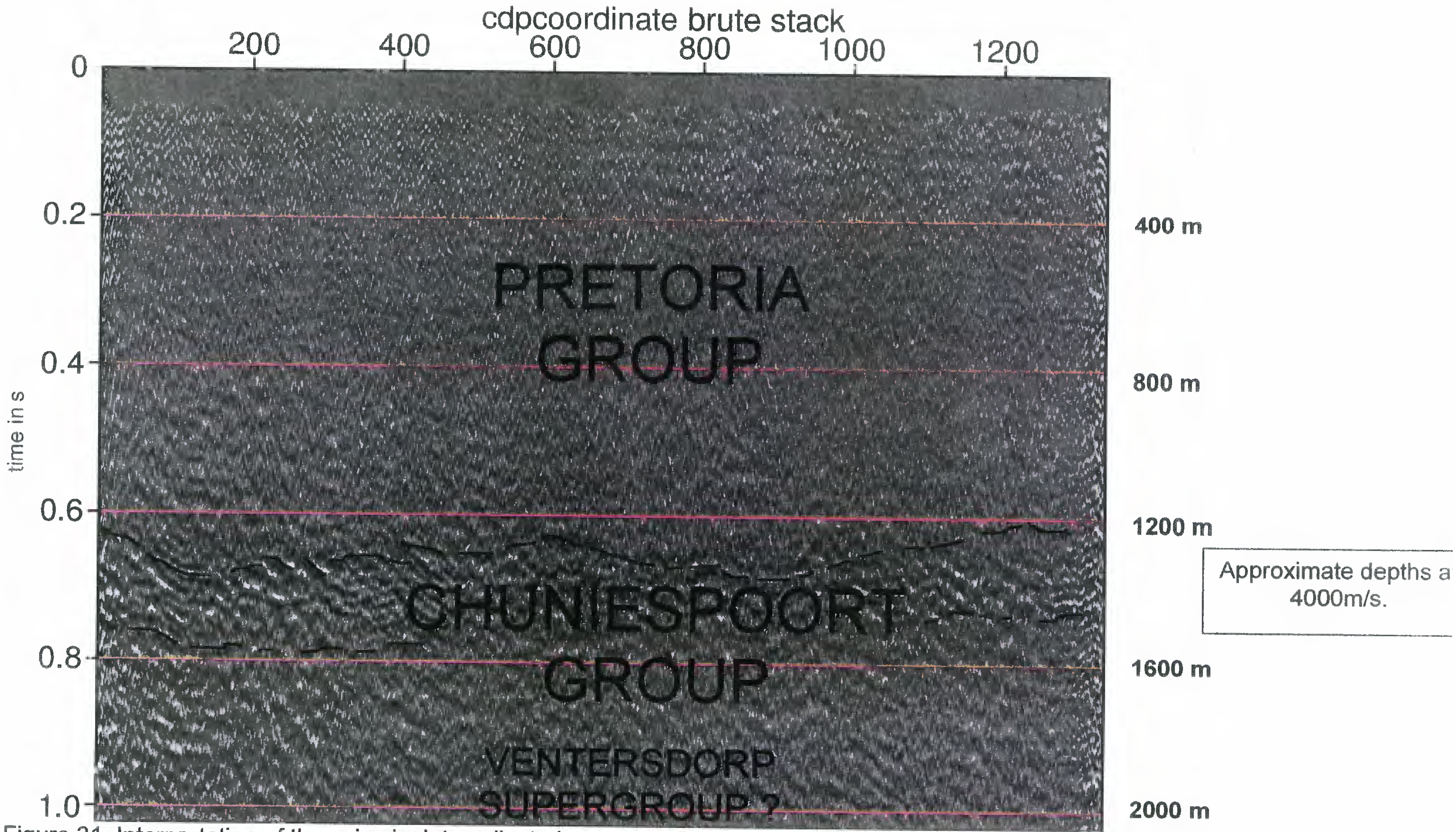

Figure 31. Interpretation of the seismic data collected.

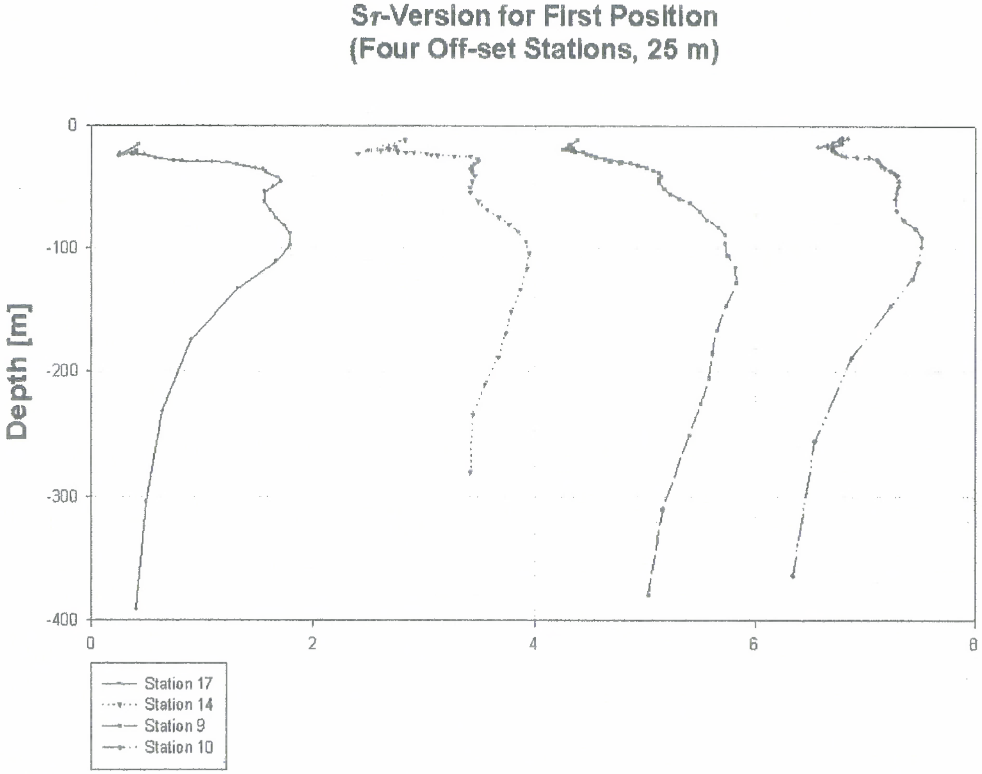

Figure 33(a). Results measured at the TOM 6 bore hole

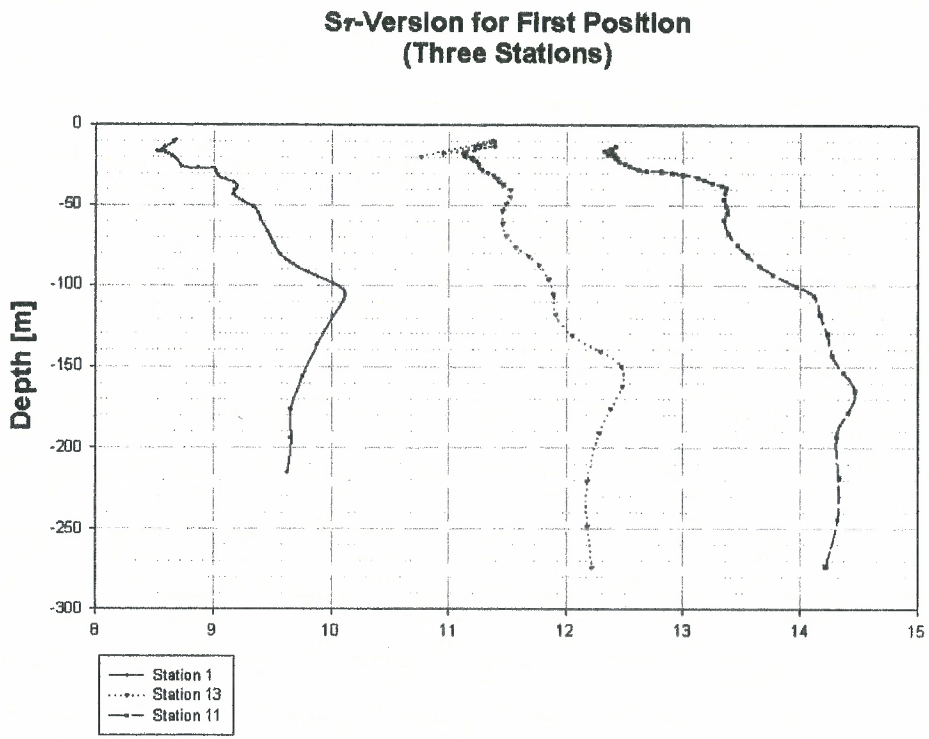

Figure 33(b). Results measured at the TOM 6 bore hole.

Theoretical S_T-Version for Two Positions, with and without IP Effect

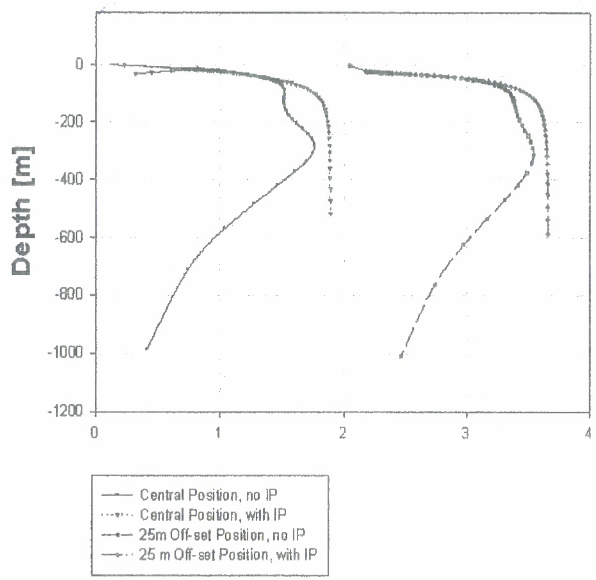

Figure 32. Time Domain Electromagnetic (TDEM) theoretical models with and without Induced Polarization effects.

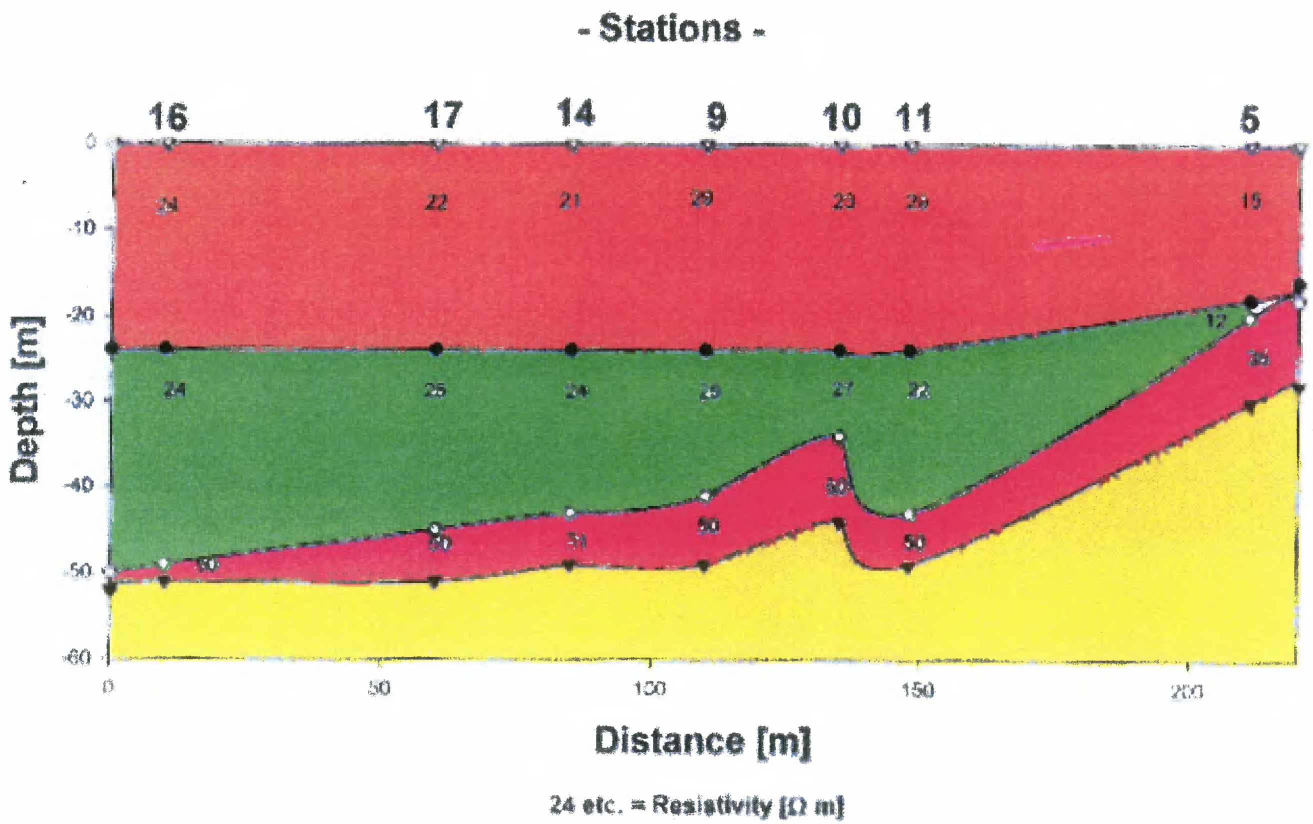

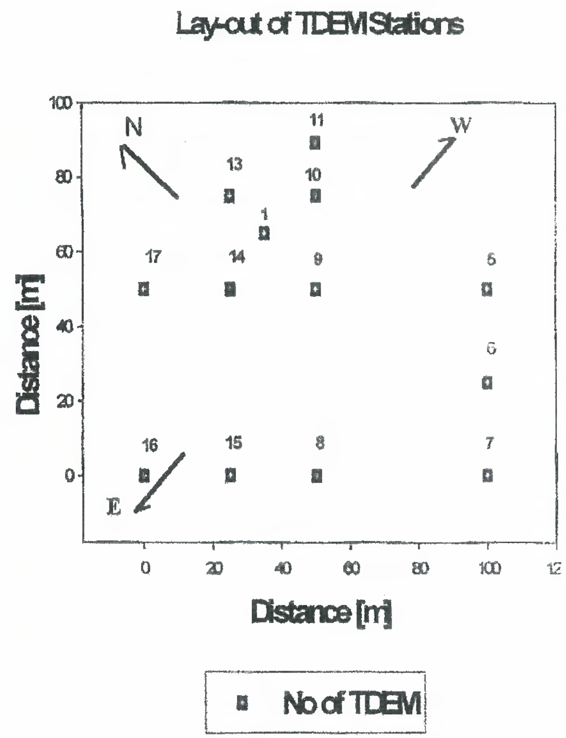

Fig. 1 Lay-out of Stations

Figure 34(a). Four layer cross-section based on resistivities as obtained at the so-called TOM 6 borehole.

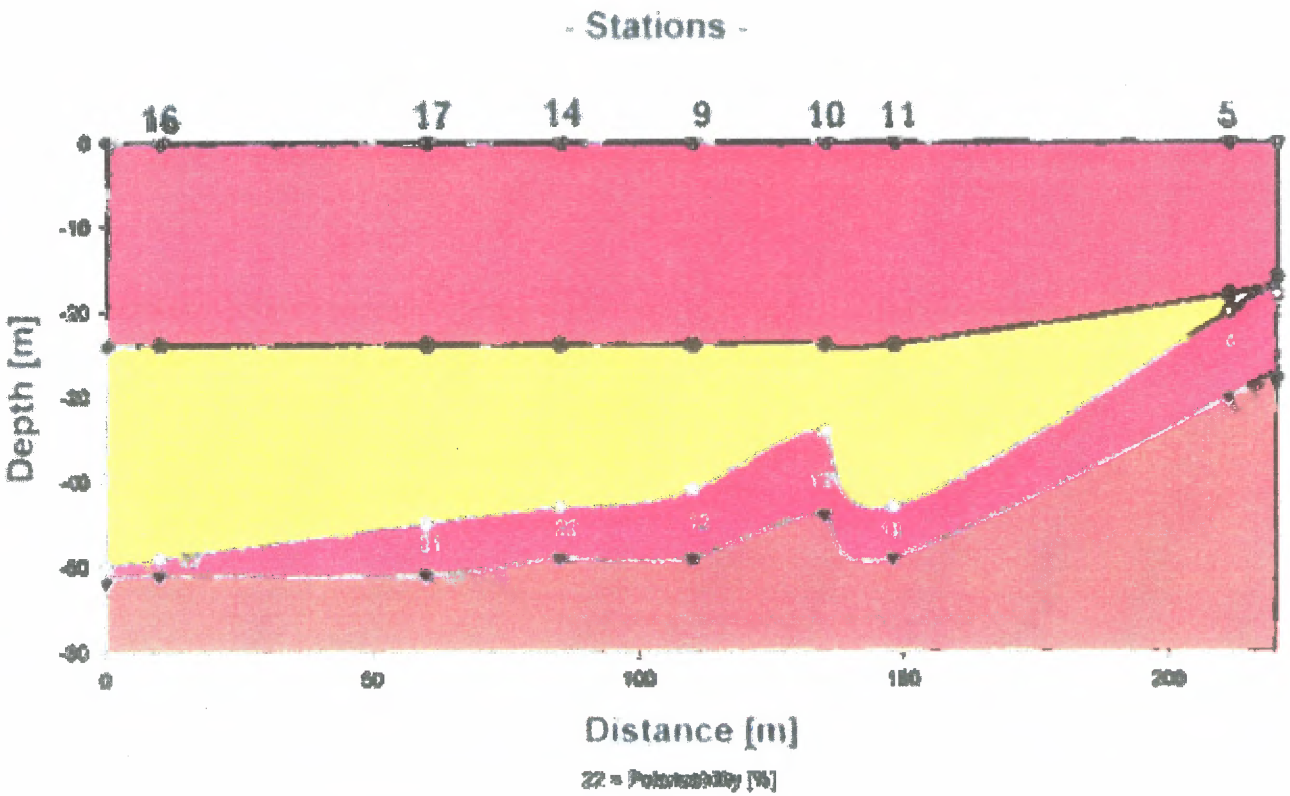

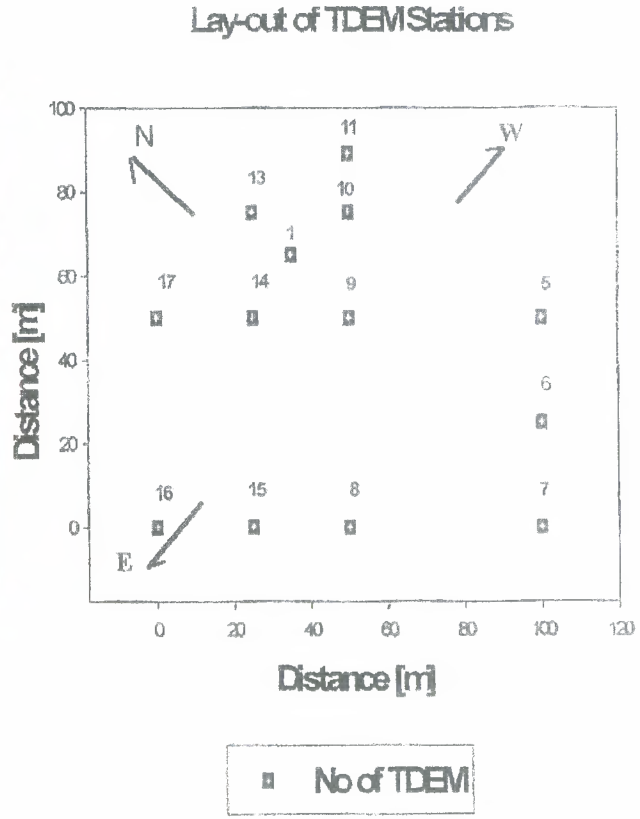

Fig. 1 Lay-out of Stations

Figure 34 (b). Four layer earth depicting the third layer to have appreciable IP effects, possibly due to the presence of hydrocarbons at a depth between 20 and 40 metres.

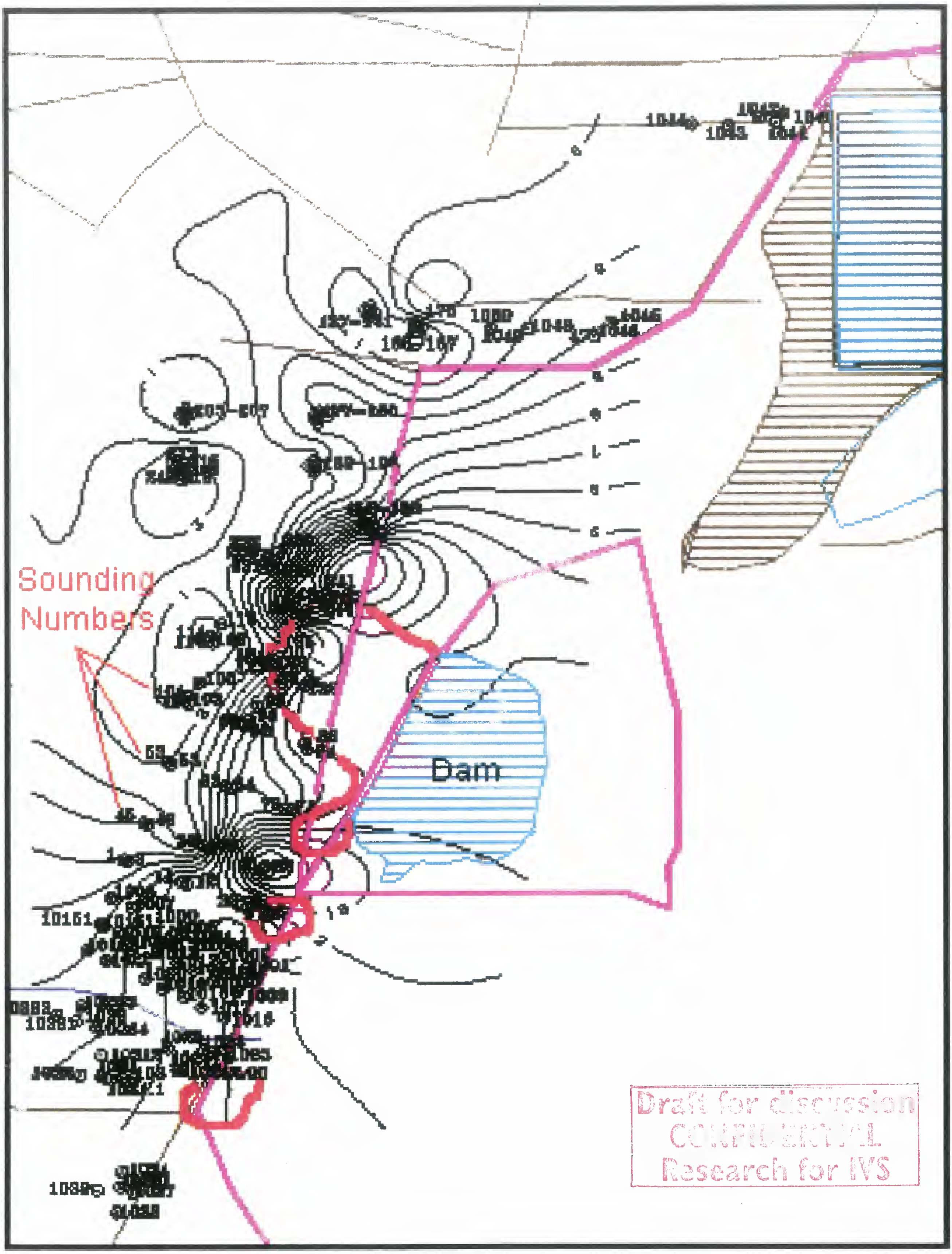

Figure 35. Time domain electromagnetic (TDEM) sounding positions in relation to Dam 10 and the existing Waste (slag) dump. The numbers refer to the sounding numbers. The contours represent the calculated induced polarization (IP) effect that can be ascribed to amongst others the presence of hydrocarbons.

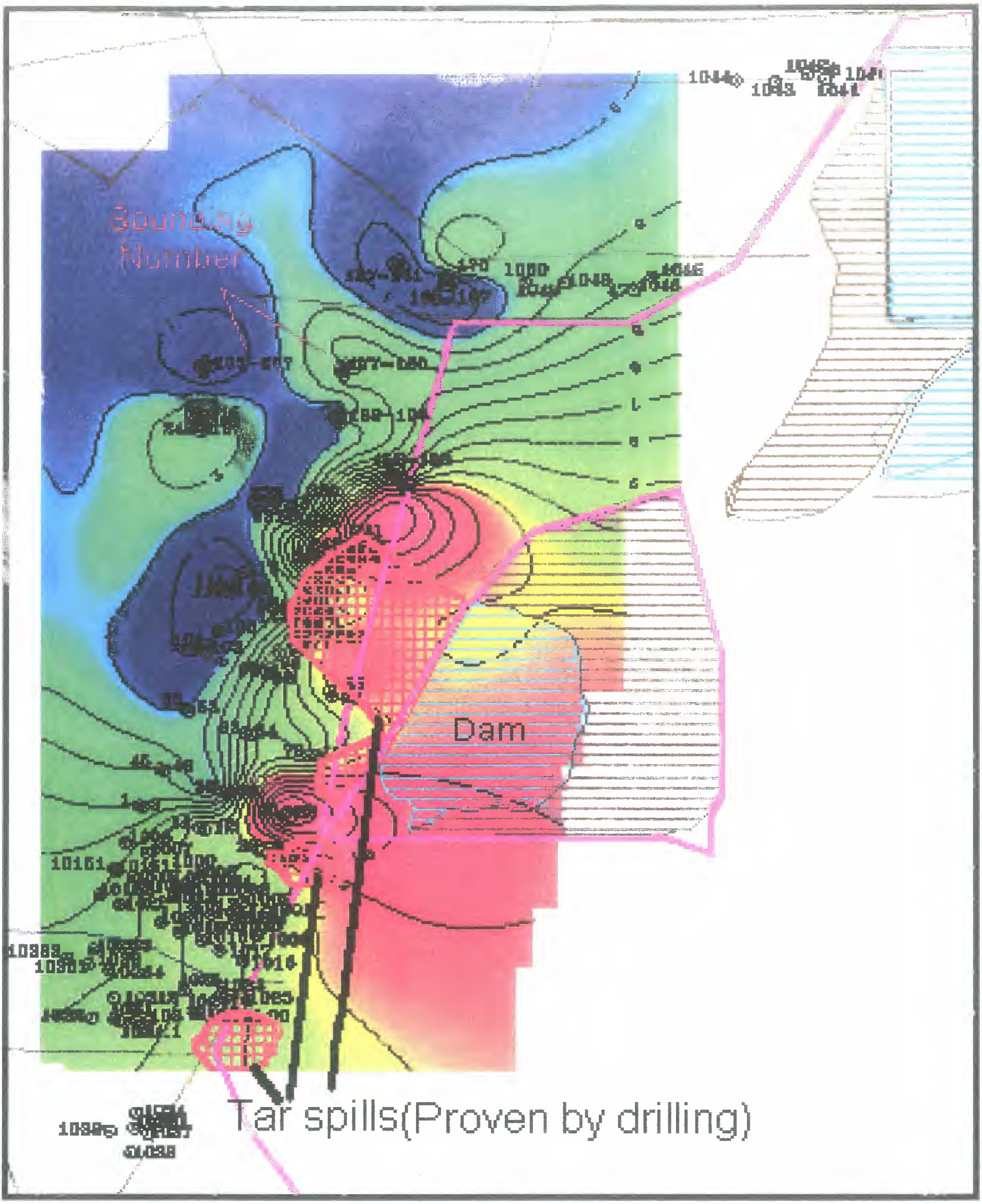

Figure 36. Percentage IP effect overlain on the infra structure map and the localities of DNAPL pools as established by drilling. The transient EM sounding positions are also indicated.

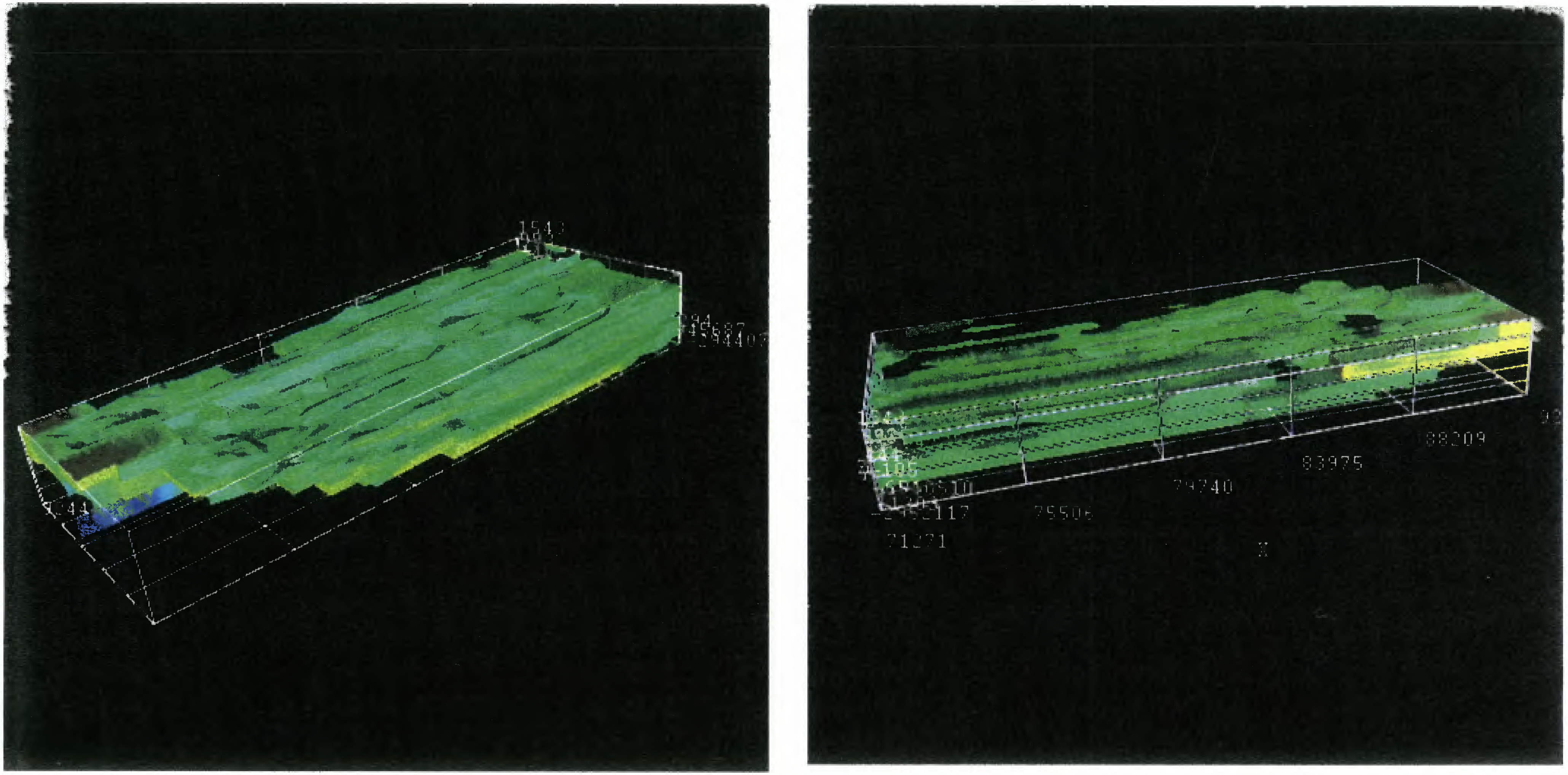

Figure 37 (a) and (b). Three-dimensional synthesised model for the area based on Phase 1 geophysical and geological data. Figure 37(a) views the model from the north east and (b) from the south.

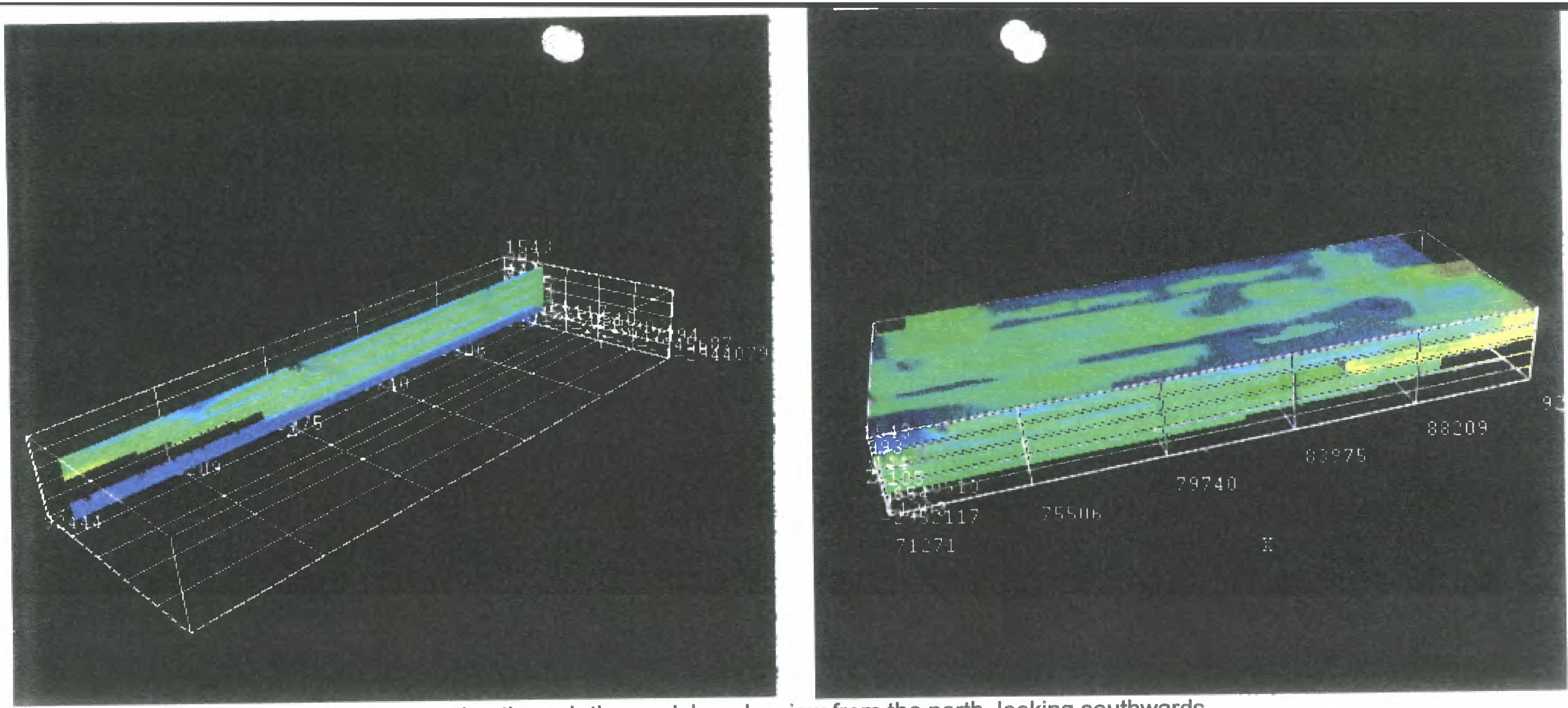

Figure 38. Montage of a cross section through the model and a view from the north, looking southwards.

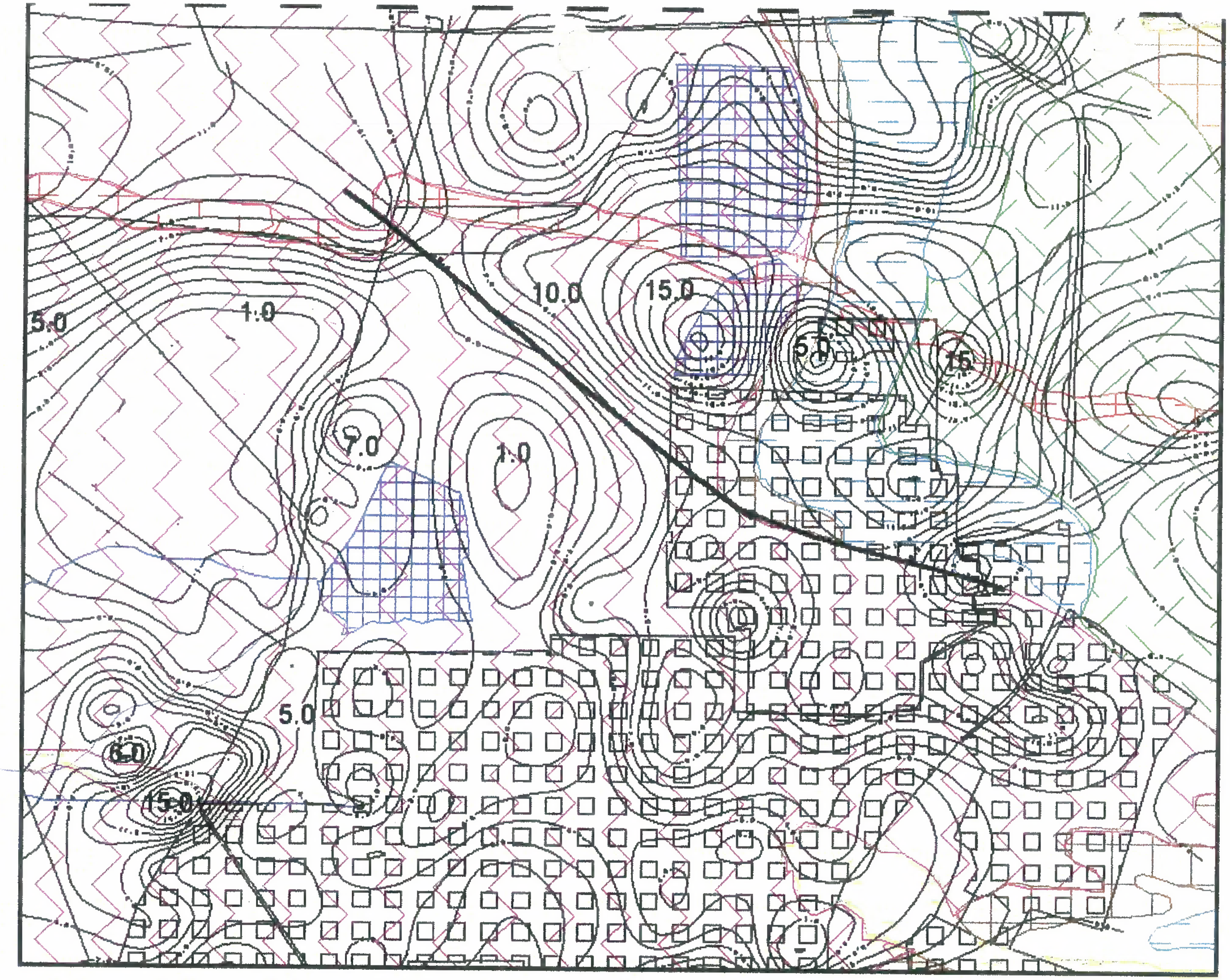

Figure 39. Overburden thickness contours overlain on the infra structure and geology for the area surrounding the waste Dumps and evaporation dams.

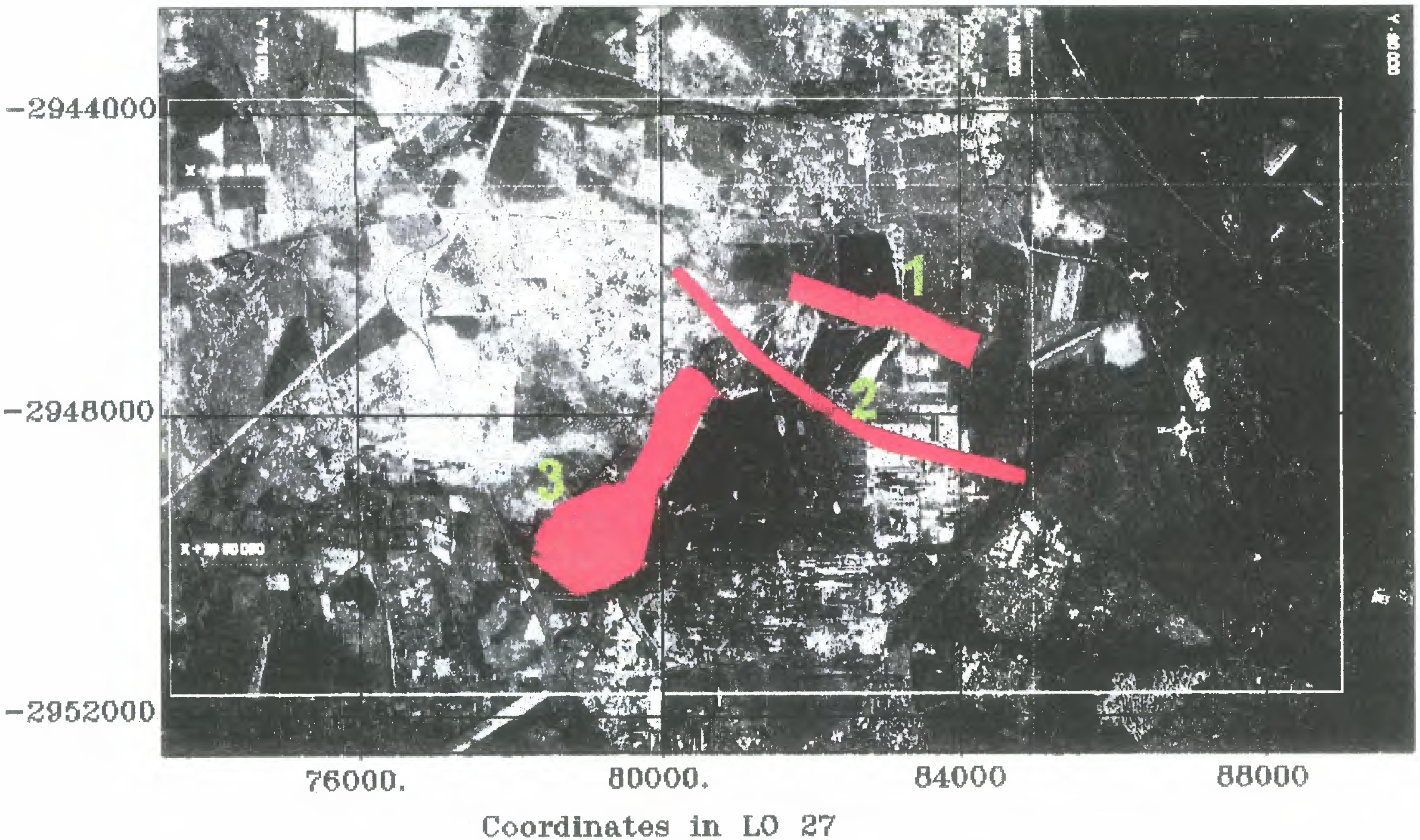

Figure 40. Vulnerable areas where DNAPL and soluble components there-off could move into the groundwater.

APPENDIX B

INSTRUMENT AND AIRCRAFT SPECIFICATIONS

APPENDIX B

The Council for Geoscience (CGS) in collaboration with Southern Exploration Surveys (SES) have developed an ultralight airborne geophysical platform to perform airborne geophysical surveys cost effectively. At the moment only magnetometer and multi-channel gamma-ray spectrometer measurements are performed routinely while an electromagnetic apparatus is under development to measure ground conductivity. An airborne near infra ref (NIR) spectrometer to determine surface mineral compositions is also under development.

EQUIPMENT DESCRIPTION

The survey will be undertaken using the following equipment:

Aircraft: The aircraft is a Jabiru 3-axis ultralight specifically modified for airborne geophysical surveys. The ground speed during survey flying is approximately 130 km per hour. As no inspection of the site has been done by the CGS, the final flying height will be decided after site inspection on arrival. It is accepted that the flying height should be as low as possible, with the pilot making the final decisions based on safety considerations. The CGS reserves the right to inspect an area before committing themselves to an airborne survey.

Magnetometer: Geometrics Cs vapour with an instrument resolution of 0.01 nT and a total noise envelope on collected airborne data not exceeding 0.5 nT sampling at ten times a second.

Spectrometer: A Bicron 4l NaI(Tl) detector with ancillary equipment, in an onboard PC. The system records 512 channels of data between 0 and 5.12 MeV, allowing the resolution of all natural gamma energies and cosmic windows (this can be adjusted to focus on specific nuclides). The spectrometer system allows automatic energy stabilization. This quote includes basic mapping of the ^{40}K, ^{214}Bi (^{238}U-^{226}Ra series), ^{208}Tl (^{232}Th series) and total count (0.4-2.8 MeV) channels to percentage K and U and Th in ppm. The data are corrected for altitude, background and cosmic radiation and the individual channels are corrected for Compton scattering. Specialist processing can be done at an extra cost.

Positioning: A SATLOC real-time differential GPS recording once a second to an accuracy of less than 1 m in x and y and 3 m in Z is utilized. The data is recorded digitally. This system does not require a base station for differential correction. It records its position relative to WGS84 Spheroid. This can be converted, if required. At the start and end of each flight, the pilot will fly over a known point to verify the GPS position. This position is plotted out after every day.

Navigation: This is controlled by the SATLOC GPS. A navigation light bar guides the pilot throughout the survey and is pre-programmed via the mission control software.

Altimeter: A highly focused laser altimeter is utilized. The altimeter is linear throughout its range and self calibrating. Calibration flights are therefore not necessary.

Ground Station Magnetometer: A Geometrics G856AG or Geotron G5 is utilized for sunspot monitoring and for diurnal correction. The data is logged every 10 seconds. Only the low frequency component is used from the ground station data for diurnal removal, and final leveling is done utilizing the tie line information. Micro-leveling can be applied to the final grid.

Data Acquisition: This is accomplished directly onto an on-board PC 104 with solid state memory. All data is merged using GPS time as the constant which is common to all collected data. Time is controlled on the PC by a stand-alone Garmin GPS linked directly to the PC.

<u>APPENDIX C</u>

TIME DOMAIN EM RESULTS

FOR

TOM 6

AND

LARGER STUDY AREA

TOM 6 RESULTS

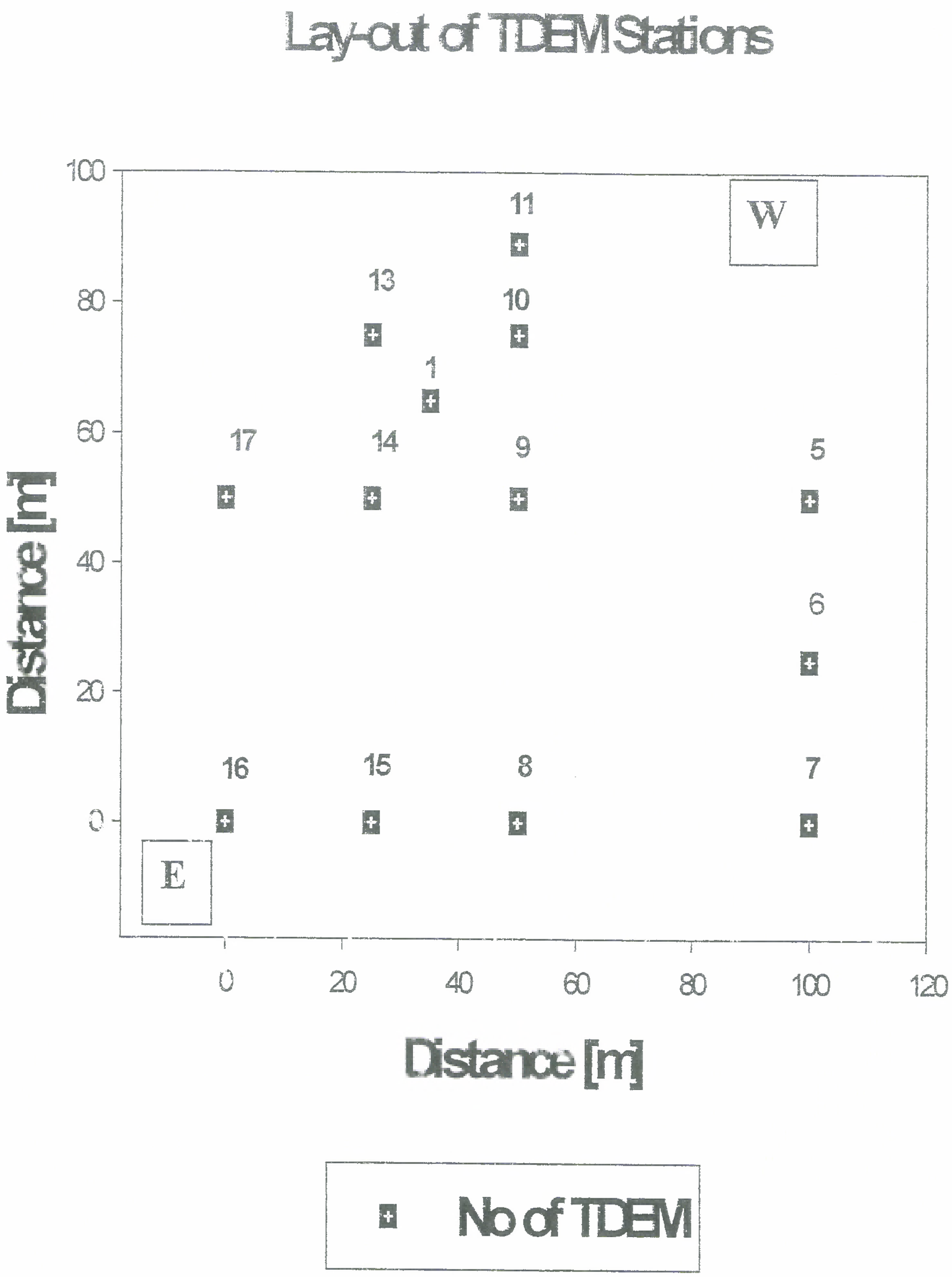

Fig. 1 Lay-out of Stations

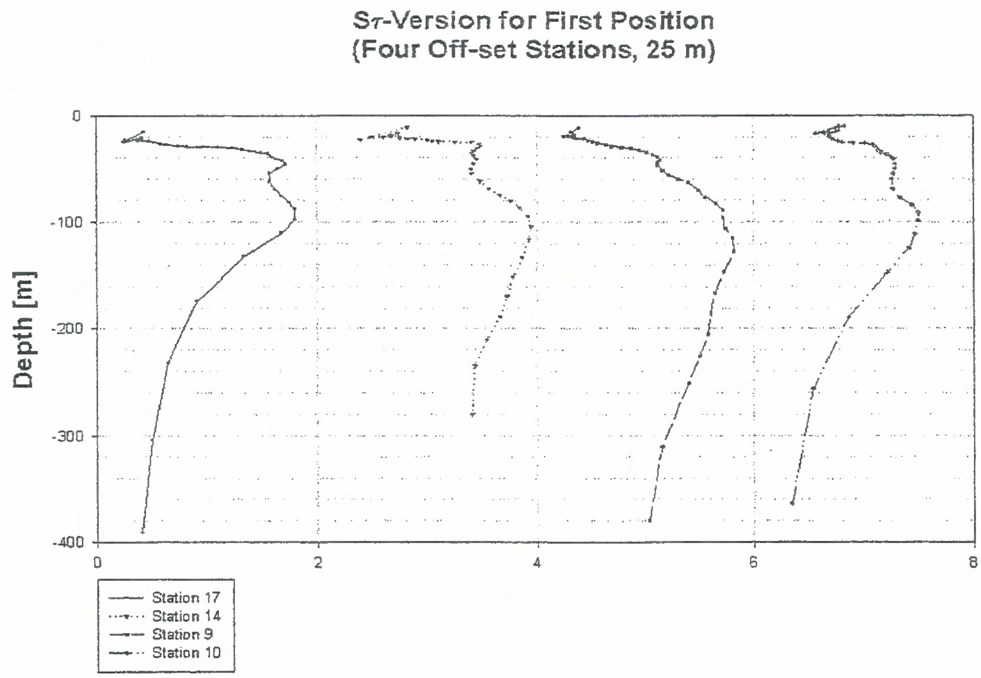

Fig. 2 Sτ curves of field data for the first stations, off-set by 25 m from the center of the loop

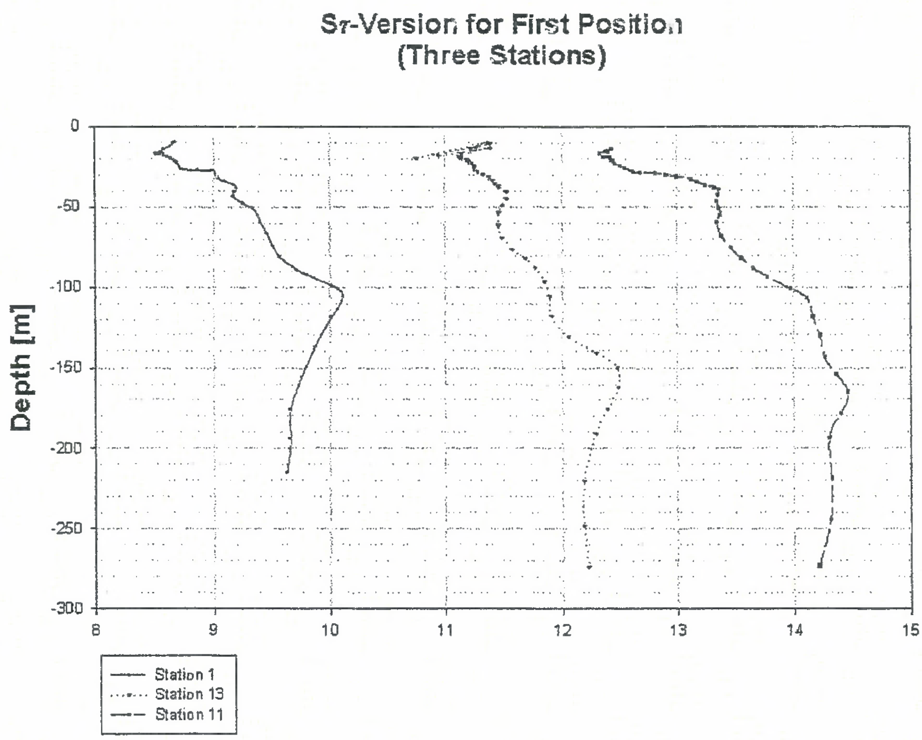

Fig. 3 Sτ curves of field data for three stations from positions close to the center of the loop

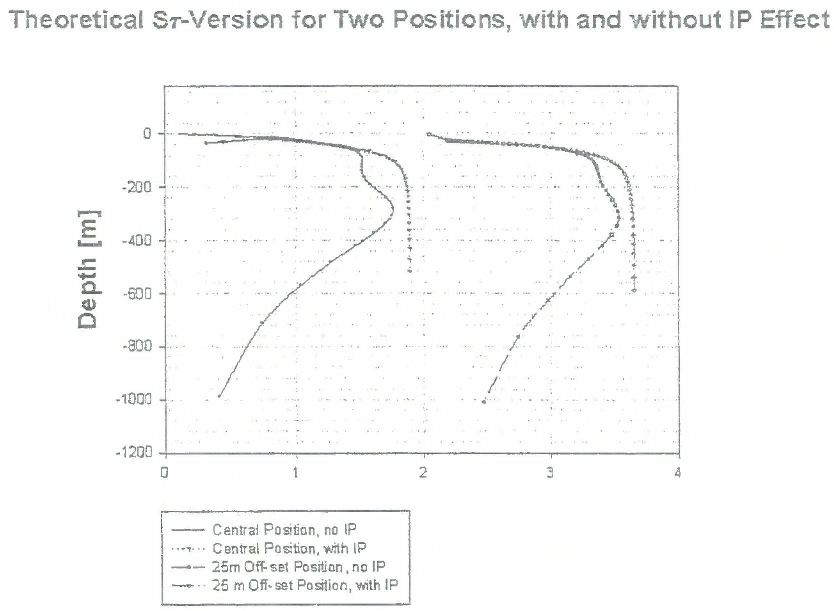

Fig. 4 Theoretical Sτ curves for a central position and a 25m off-set position, with and without IP effect

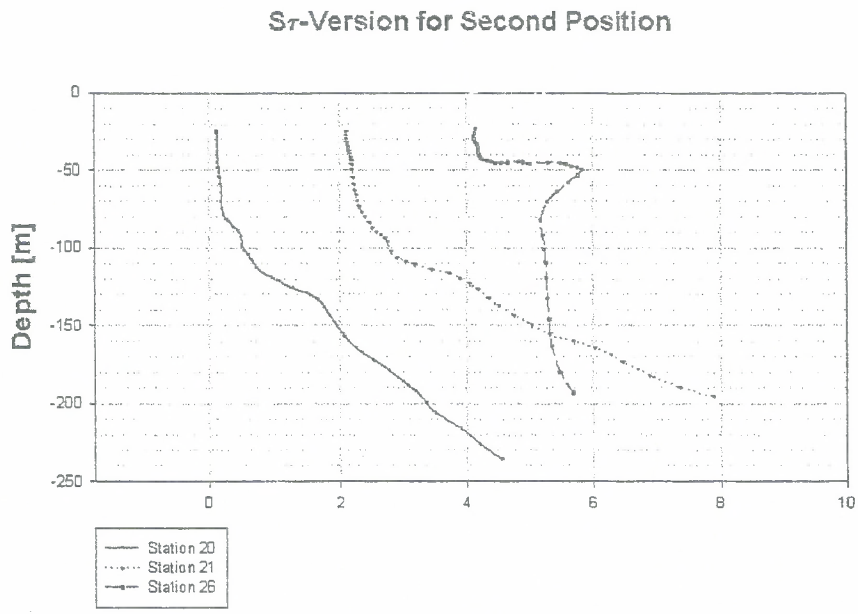

Fig. 5 Sτ curves from field data for three stations in area 2

TDEM 1

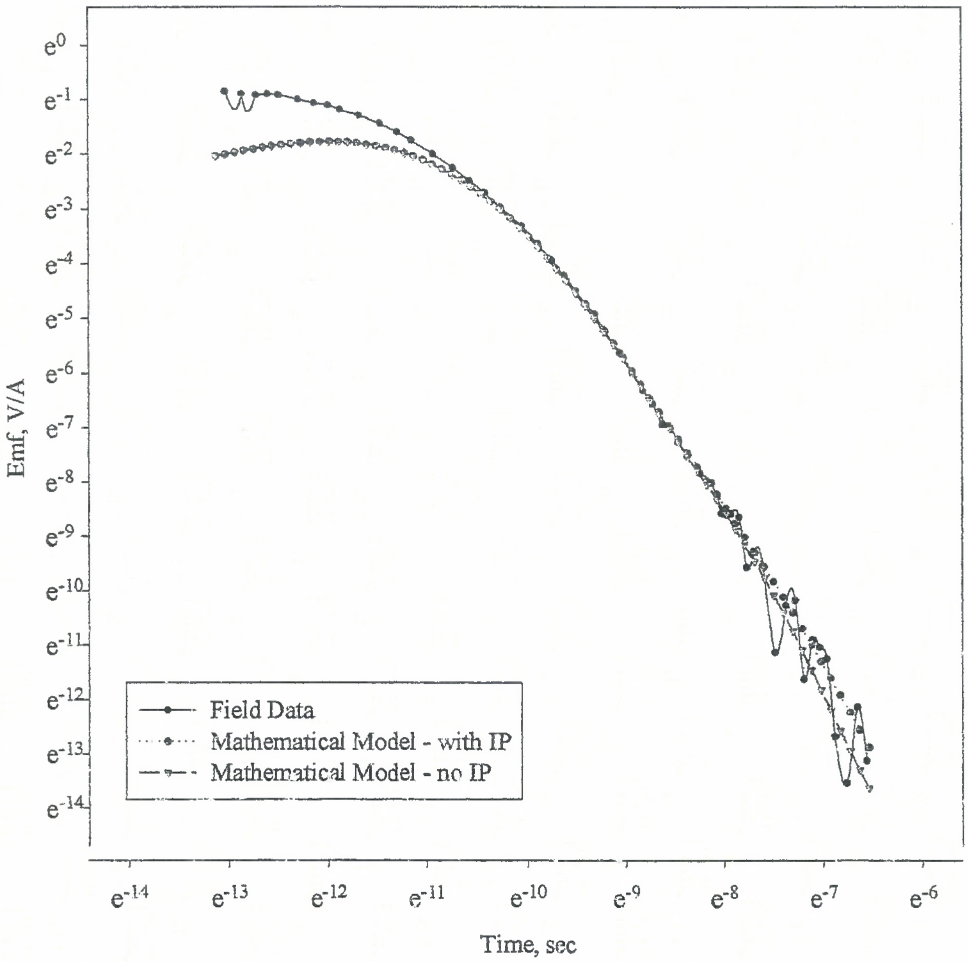

Parameters of cross-section

№ of layers	ρ resistivity (Ω·m)	h thickness, m	τ decay constant (msec)	η polarizability (%)
1	28.3	25	-	-
2	24	18	0.05	4
3	51	8	0.45	11
4	115	80	-	-

Fig. 6 Comparison of field data with mathematical modeling for station no 1

TDEM 9

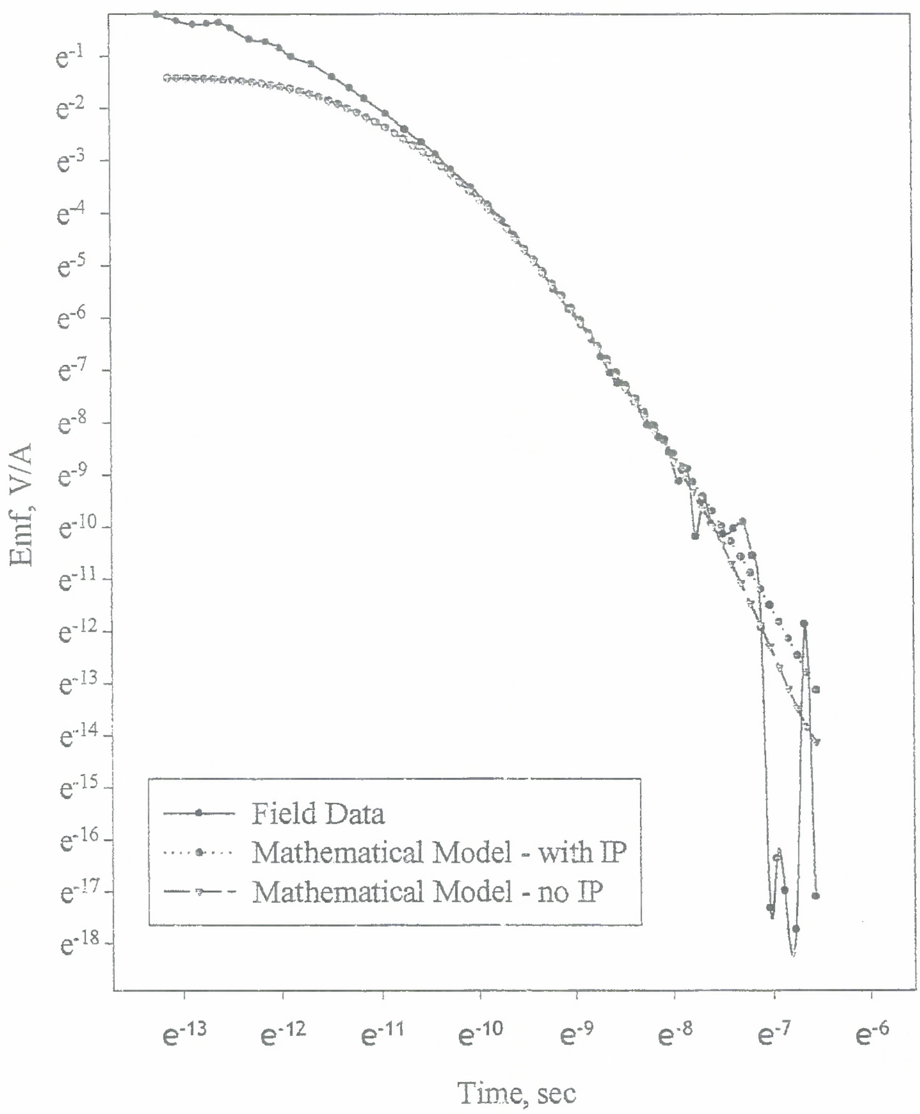

Parameters of cross-section

№ of layers	ρ resistivity (Ω·m)	h thickness, m	τ decay constant (msec)	η polarizability (%)
1	29	24	-	-
2	25	17	0.05	4
3	50	86	0.42	12
4	115	82	-	-

Fig. 7 Comparison of field data with mathematical modeling for station no 9

TDEM 10

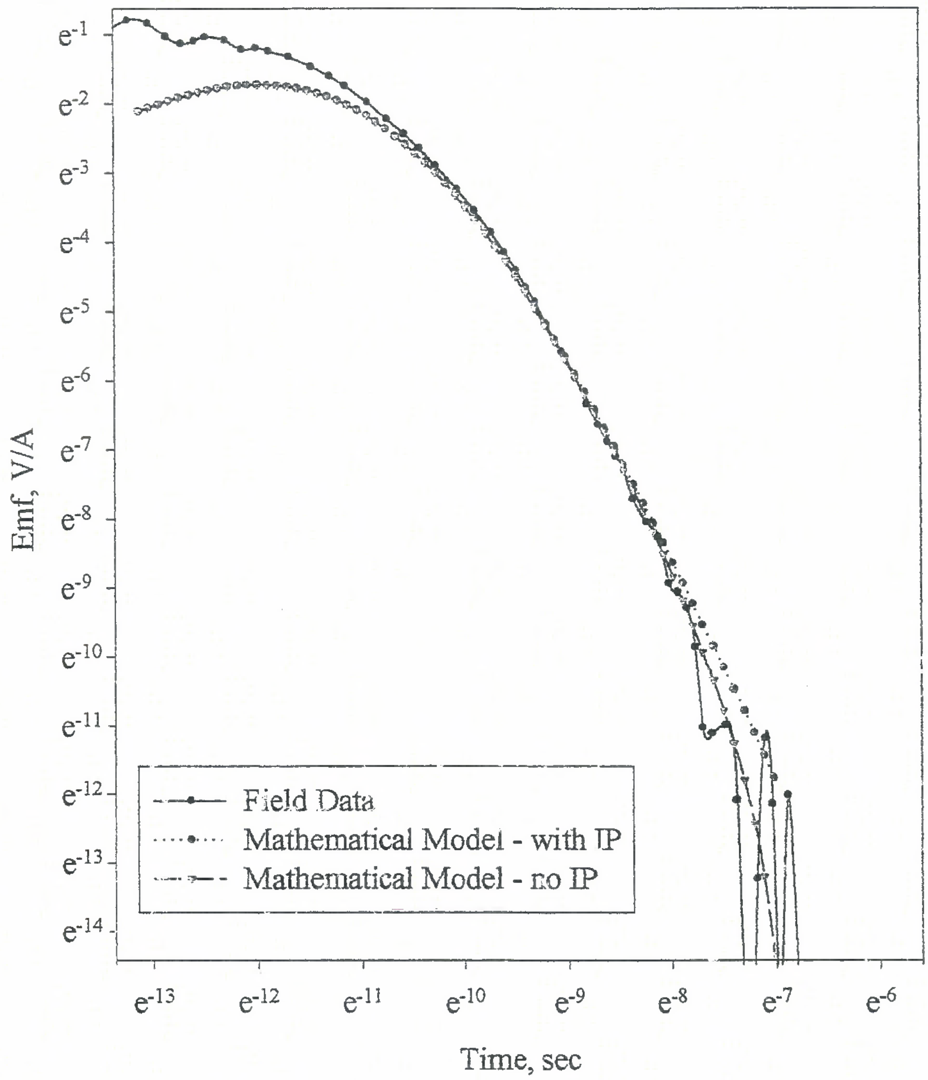

Parameters of cross-section

№ of layers	ρ resistivity (Ω·m)	h thickness, m	τ decay constant (msec)	η polarizability (%)
1	23.3	24	-	-
2	27	10	0.05	4
3	50	10	0.40	11-12
4	165	82	-	-

Fig. 8 Comparison of field data with mathematical modeling for station no 10